

$\text{N}_2\text{H}^+(1-0)$ survey of massive molecular cloud cores

L. Pirogov¹, I. Zinchenko^{1,2,3}, P. Caselli⁴, L. E. B. Johansson⁵, P. C. Myers⁶

¹ Institute of Applied Physics of the Russian Academy of Sciences, Ulyanova 46, 603950 Nizhny Novgorod, Russia
e-mail: pirogov@appl.sci-nnov.ru

² Nizhny Novgorod University, Gagarin av. 23, 603950 Nizhny Novgorod, Russia

³ Helsinki University Observatory, Tähtitorninmäki, P.O. Box 14, FIN-00014 University of Helsinki, Finland

⁴ INAF – Osservatorio Astrofisico di Arcetri, Largo E. Fermi 5, I-50125 Firenze, Italy

⁵ Onsala Space Observatory, S-43992, Onsala, Sweden

⁶ Harvard-Smithsonian Center of Astrophysics, 60 Garden Street, Cambridge, MA 02138, USA

Abstract. We present the results of $\text{N}_2\text{H}^+(1-0)$ observations of 35 dense molecular cloud cores from the northern and southern hemispheres where massive stars and star clusters are formed. Line emission has been detected in 33 sources, for 28 sources detailed maps have been obtained. Peak N_2H^+ column densities lie in the range: $3.6 \cdot 10^{12} - 1.5 \cdot 10^{14} \text{ cm}^{-2}$. Intensity ratios of (01–12) to (23–12) hyperfine components are slightly higher than the LTE value. The optical depth of (23–12) component toward peak intensity positions of 10 sources is $\sim 0.2 - 1$. In many cases the cores have elongated or more complex structures with several emission peaks. In total, 47 clumps have been revealed in 26 sources. Their sizes lie in the range 0.3–2.1 pc, the range of virial masses is $\sim 30 - 3000 M_\odot$. Mean N_2H^+ abundance for 36 clumps is $5 \cdot 10^{-10}$. Integrated intensity maps with aspect ratios < 2 have been fitted with a power-law radial distribution $\sim r^{-p}$ convolved with the telescope beam. Mean power-law index for 25 clumps is close to 1.3. For reduced maps where positions of low intensity are rejected mean power-law index is close to unity corresponding to the $\sim r^{-2}$ density profile provided N_2H^+ excitation conditions do not vary inside these regions. In those cases where we have relatively extensive and high quality maps, line widths of the cores either decrease or stay constant with distance from the center, implying an enhanced dynamical activity in the center. There is a correlation between total velocity gradient direction and elongation angle of the cores. However, the ratio of rotational to gravitational energy is too low ($4 \cdot 10^{-4} - 7.1 \cdot 10^{-2}$) for rotation to play a significant role in the dynamics of the cores. A correlation between mean line widths and sizes of clumps has been found. A comparison with physical parameters of low-mass cores is given.

Key words. Stars: formation – ISM: clouds – ISM: molecules – Radio lines

1. Introduction

It is well-known that stars in some cases are formed in clusters and isolation in others, however, the reasons of such a dichotomy are far from being understood at present. The number of stars depends apparently on physical parameters of dense molecular cloud cores where stars are formed. It is known, in particular, that clusters are formed in the most massive and turbulent cores. High-mass stars are encountered solely in such cores. An important feature of massive cores is their clumpy structure which extends from large scales down to the smallest ones even unresolved by present-day telescopes. An existence of small-scale clumpiness is implied, for example, by 1–2 orders of magnitude difference between mean densities and densities derived from multitransitional analysis (e.g. Bergin et al. 1996, Zinchenko 1995, Zinchenko et al. 1998); by the absence of significant broadening of presumably very optically thick CS lines as compared to the rarer C^{34}S isotopomer lines (Zinchenko et al. 1998); by the hyperfine intensity ratios

anomalies in HCN (Pirogov 1999) and ammonia (Stutzki & Winnewisser 1985) in warm clouds. The degree of small-scale clumpiness is probably related to the number of newborn stars.

Important parameters for describing evolution of star forming cores in modern theoretical models are radial dependences of density and velocity dispersion in envelopes that surround newborn stars. A popular model for massive star formation is based on the logatropic equation of state which incorporates non-thermal gas motions (McLaughlin & Pudritz 1996). It results in the $\sim r^{-1}$ density distribution. Velocity dispersion in this model is nearly constant in the center and rises with distance in the outer regions as $\sim r^{1/3}$. In contrast, the standard theory of low-mass star formation from a singular isothermal sphere (Shu 1977) predicts the $\sim r^{-2}$ density profile in the static outer envelope. Both models predict $\sim r^{-3/2}$ and $\sim r^{-1/2}$ density and velocity profiles, respectively, for the regions involved in free-falling collapse (Shu 1977, McLaughlin & Pudritz 1997). Therefore, studies of density and velocity dispersion profiles in the cores are essential for discrimination between different theoretical models and for determination of their dynamical status.

Recently, density structure of large samples of objects have been explored in several studies. Analysis of dust continuum emission in low-mass cores where stars are formed mostly in isolation, reveals a density power-law index of $\alpha \sim 1.5 - 2$ (e.g. Motte & André 2001, Shirley et al. 2002) being more or less in accordance with the isothermal sphere model. Dust continuum emission studies in high-mass star forming regions have resulted in the following power-law indices: $\langle\alpha\rangle = 1.6(0.5)$ (Beuther et al. 2002) and $\langle\alpha\rangle = 1.8(0.4)$ (Mueller et al. 2002), while molecular multi-line modeling of several massive star forming regions (Van der Tak et al. 2000) gave somewhat lower values: $\alpha = 1.0 - 1.5$.

In their study of velocity dispersion profiles in low-mass cores, Goodman et al. (1998) found nearly constant velocity dispersion within so-called “coherent regions” with sizes of ~ 0.1 pc and a rise of velocity dispersion in the outer regions with power-law index $\gtrsim 0.2$, which is more consistent with the logatropic model. In contrast, molecular line studies of high-mass cores show highly non-thermal lines of decreasing widths with distance from center (Zinchenko 1995, Lapinov et al. 1998, Fontani et al. 2002), which apart from optical depth effects could imply a higher degree of gas dynamical activity in central regions.

Recently, about 60 nearby low-mass cores were mapped in the $N_2H^+(1-0)$ line (Caselli et al. 2002, hereafter Paper I). As a result, a number of physical parameters including density and velocity dispersion profiles were derived. N_2H^+ was chosen as a tracer of quiescent high density gas (critical density for excitation of the $J = 1-0$ transition at a kinetic temperature of 40 K is $4.4 \cdot 10^5 \text{ cm}^{-3}$). An advantage of the $N_2H^+(1-0)$ transition is the hyperfine structure which enables a reliable determination of the optical depth and improves estimates of related physical parameters of the dense gas that surrounds young stars. It is known that the $N_2H^+(1-0)$ lines have relatively strong intensities and moderate ($\tau \sim 1$) optical depths both in cold and warm clouds (Womack et al. 1992) associated with low-mass and high-mass star forming regions, respectively. The goal of the present study is to derive physical parameters for a representative sample of dense cores in high-mass star forming regions from observations in the $N_2H^+(1-0)$ line. The derived parameters will be compared with those of low-mass cores (Paper I) to help to understand the details of the star formation process.

A sample list for the study has been taken from the ammonia database compiled by P. Myers and co-workers (Jijina et al. 1999) where data on cluster existence is included. This list overlaps with a sample of massive cores earlier mapped in CS, both in the northern and southern hemispheres (Zinchenko et al. 1994, 1995, 1998; Juvela 1996). In the present paper we give the results of $N_2H^+(1-0)$ observations towards a sample of 35 massive dense cores where star formation in clusters is going on. Their physical parameters including density and velocity dispersion profiles are derived and compared with parameters of low-mass cores (Paper I).

2. Observations

The $N_2H^+(1-0)$ observations at the frequency 93.2 GHz have been done in April, 2000 at 20-m OSO radiotelescope and in

February, 2001 at 15-m SEST radiotelescope. The observing parameters are given in Table 1.

For OSO we took into account beam efficiency dependence on source elevation and give an average value. We also give the ranges of system temperatures which depend on source elevation and weather conditions. At OSO we used both a filterbank spectrum analyzer (256 channels) and autocorrelator (1600 channels) while at SEST an acousto-optical spectrum analyzer (1000 channels) was used. Pointing was regularly checked by SiO maser observations and usually was better than $5''$.

Table 1. $N_2H^+(1-0)$ observing parameters.

Telescope	$\Delta\Theta$ ($''$)	η_{mb}	T_{sys} (K)	δV (km s^{-1})
OSO-20m	40	~ 0.5	250–500	0.8; 0.16
SEST-15m	55	0.75	200–300	0.14

The objects for observations were selected from the list of dense cores observed earlier in the CS(2–1) line (Zinchenko et al. 1994, 1995, 1998; Juvela 1996) as well as from the ammonia database (Jijina et al. 1999) according to the following criteria: an existence of embedded clusters of stars detected in infrared (Jijina et al. 1999, Hodapp 1994, Carpenter et al. 1993), distances to the objects not far than 5 kpc and an existence of extended CS or NH_3 emission regions ($> 2'$) in order to get detailed $N_2H^+(1-0)$ maps. In the cases of no data on the clusters existence, the sources with high IR-luminosities were selected ($L > 10^4 L_\odot$), which can be an indirect indication of cluster (Jijina et al. 1999). In total, 35 objects that satisfy these criteria were selected. The source list with coordinates and distances is given in Table 2. The number of points per map and the names of associated objects are also given. Mapping has been done with $20''$ grid spacing (Nyquist sampled maps) with the exception of S 187, G 133.69 and S 153 for which the spacing was $40''$ (beam sampled maps).

3. Results

3.1. Integrated intensity maps

The $N_2H^+(1-0)$ emission has been detected in 33 of 35 sources (except LkH α 101 and LkH α 25). Maps of intensities integrated over all hyperfine components for 31 object are given in Fig. 1. The maps of AFGL 490 and G 142.00 (which actually belong to a single molecular complex), S 88B, G 267.94 and G 305.36 have not been completed (the latter two are not shown in Fig. 1). The maps of S 187, G 133.69 and AFGL 6366 each consist of two separated clumps at the 30% peak intensity level. Some others (e.g. S 255, G 316.77, G 345.41, G 351.41) contain intensity peaks separated at the half maximum intensity level. The maps of RNO 1B, NGC 281, G 173.48, S 76E, G 270.26 indicate spherical symmetry while others demonstrate elongated, curved or more complex structures. Per 4 and L 1251T4 show the most narrow and weak lines and actually belong to low-mass star forming cores (see Paper I). The

Table 2. Source list.

Source	RA (1950) (^h ^m ^s)	Dec (1950) ([°] ['] ^{''})	<i>D</i> (kpc)	Points per map	Associated objects
RNO 1B	00 33 53.3	63 12 32	0.85 ^a	70	L1287, G 121.30+0.66, IRAS 00338+6312
NGC 281	00 49 29.2	56 17 36	3.5 ^b	34	S184, G 123.07-6.31
S 187	01 19 58.0	61 34 32	1.0 ^c	67	G 126.68-0.83
G 133.69+1.22	02 21 40.8	61 53 26	2.1 ^d	52	W3
S 199	02 57 36.9	60 17 32	2.1 ^d	46	IC1848, AFGL 4029
S 201	02 59 22.4	60 16 12	2.1 ^e	41	AFGL 437, G 138.50+1.64
AFGL 490	03 23 34.0	58 33 47	0.9 ^f	18	
G142.00+1.83	03 23 41.0	58 36 52	0.9 ^f	37	AFGL 490
Per 4	03 26 12.1	31 17 13	0.35 ^g	78	
LkHα101	04 26 57.3	35 09 56	0.8 ^h	9	AFGL 585, S222
G 173.48+2.45	05 35 51.3	35 44 16	2.3 ^d	54	S231
G 173.58+2.44	05 36 06.3	35 39 21	2.3 ^d	41	
AFGL 6366	06 05 40.1	21 31 16	2.0 ⁱ	50	S247
S 255	06 09 58.2	18 00 17	2.5 ^d	67	AFGL 896
LkHα25	06 37 59.5	09 50 53	0.8 ^j	1	AFGL 4519S, NGC 2264, S273
S 76E	18 53 47.0	07 49 25	2.1 ^k	61	G40.50+2.54
S 88B	19 44 41.4	25 05 17	2.0 ^d	25	
DR 21	20 37 13.5	42 12 15	3.0 ^l	56	W75
S 140	22 17 41.1	63 03 44	0.9 ^d	82	L1204
L 1251T4	22 27 10.2	74 58 00	0.35 ^m	119	
S 153	22 56 42.0	58 28 45	4.0 ^d	42	
G 264.28+1.48	08 54 39.0	-42 53 30	1.4 ⁿ	43	
G 265.14+1.45	08 57 36.3	-43 33 38	1.7 ⁿ	64	
G 267.94-1.06	08 57 21.7	-47 19 04	0.7 ⁿ	9	
G 268.42-0.85	09 00 12.1	-47 32 07	1.3 ⁿ	60	
G 269.11-1.12	09 01 51.6	-48 16 42	2.6 ⁿ	53	
G 270.26+0.83	09 14 58.0	-47 44 00	2.6 ⁿ	27	
G 285.26-0.05	10 29 36.8	-57 46 40	4.7 ⁿ	59	
G 291.27-0.71	11 09 42.0	-61 01 55	2.7 ^o	104	
G 294.97-1.73	11 36 51.6	-63 12 09	1.2 ⁿ	39	
G 305.36+0.15	13 09 21.0	-62 21 43	4.2 ⁿ	18	
G 316.77-0.02	14 41 10.4	-59 35 50	3.1 ^p	136	
G 345.01+1.80	16 53 17.3	-40 09 23	2.1 ^p	103	RCW 116
G 345.41-0.94	17 06 02.2	-41 32 06	2.8 ^p	71	RCW 117
G 351.41+0.64	17 17 32.3	-35 44 03	1.7 ^q	88	NGC 6334I

^a Yang et al. (1991), ^b Martin & Henning (1992), ^c Fich & Blitz (1984), ^d Blitz et al. (1982), ^e assumed, ^f Harvey (1979), ^g Paper I, ^h Lada (1985), ⁱ Carpenter et al. (1993), ^j Snell et al. (1990), ^k Plume et al. (1992), ^l Harvey et al. (1977), ^m Toth & Walmsley (1996), ⁿ Zinchenko et al. (1995), ^o Brand & Blitz (1993), ^p Juvela (1996), ^q Neckel (1978)

clumpy structures visible in the maps of these two sources (see Fig. 1) are primarily caused by noise. The OSO and SEST beam sizes are shown in Fig. 1 on RNO 1B and G 268.42 maps, respectively.

Most of the sources have associated IRAS point sources. The positions of IRAS sources are indicated by stars and the uncertainty ellipses corresponding to 95% confidence level are also shown. In 17 objects IRAS sources lie within the half maximum level (marked by thick black lines) or coincide with a secondary intensity peak. Although there is no IRAS point source in DR 21, it is a well-known star forming molecular cloud with compact H II regions and strong extended far-infrared emission (Harvey et al. 1979) which is close in shape to the N₂H⁺(1–0) integrated intensity distribution.

Peak integrated intensities are given in Table 3. For the sources having separate clumps at the 30% level, peak intensity

for each clump is given. The uncertainties of integrated intensities have been calculated as $\Delta T_{\text{MB}} \sqrt{N_{\text{ch}}} \delta V_{\text{ch}}$, where ΔT_{MB} – noise level in channel without line (after baseline subtracting), N_{ch} – number of line channels, δV_{ch} – velocity resolution. For the sources observed at OSO we used high-resolution autocorrelator data, with the exception of S 88B for which only filterbank data are available.

3.2. N₂H⁺(1–0) line parameters and peak column densities

N₂H⁺(1–0) spectra consist of seven hyperfine components (Womack et al. 1992, Caselli et al. 1995). However, due to overlap of closely spaced components only three lines (two of which are actually triplets) have been observed in most cases (with exception of L1251 and Per4). As an ex-

Table 3. $N_2H^+(1-0)$ line parameters and LTE column densities

Source ($\Delta\alpha''$, $\Delta\delta''$)	I (K km s ⁻¹)	$T_{MB}(23-12)$ (K)	R_{12}	R_{02}	$V_{LSR}(23-12)$ (km s ⁻¹)	ΔV (km s ⁻¹)	$N(N_2H^+)$ (cm ⁻²) (10 ¹²)
RNO 1B (0,0)	27.0(0.4)	2.88(0.04)	0.66(0.01)	0.47(0.02)	-17.55(0.01)	2.39(0.03)	31.1
NGC 281 (0,0)	27.2(0.4)	2.29(0.03)	0.68(0.02)	0.48(0.02)	-30.36(0.02)	2.91(0.04)	31.2
S 187 (0,0)	6.3(0.4)	1.6(0.1)	0.68(0.07)	0.57(0.08)	-13.33(0.03)	0.91(0.06)	7.2
S 187 (120,-80)	4.9(0.4)	0.73(0.07)	0.7(0.1)	0.6(0.1)	-13.59(0.05)	1.5(0.2)	5.6
G 133.69+1.22 (160,-160)	11.7(0.7)	1.4(0.1)	0.62(0.07)	0.6(0.1)	-38.38(0.05)	1.8(0.1)	13.4
G 133.69+1.22 (40,-80)	8.0(0.7)	0.38(0.05)	1.0(0.2)	0.8(0.2)	-41.9(0.2)	3.6(0.4)	9.2
S 199 (0,-20)	9.7(0.6)	0.94(0.06)	0.64(0.07)	0.6(0.1)	-38.02(0.06)	2.3(0.2)	11.2
S 201 (40,40)	3.9(0.4)	0.26(0.03)	1.2(0.2)	0.8(0.2)	-37.3(0.1)	2.8(0.3)	4.5
AFGL 490 (-20,0)	7.6(0.6)	1.5(0.1)	0.67(0.09)	0.6(0.1)	-12.24(0.04)	1.1(0.1)	8.7
G142.00 (-20,-80)	10.9(0.7)	1.2(0.1)	0.7(0.1)	0.4(0.1)	-13.00(0.06)	1.8(0.2)	12.5
Per 4 (0,0)	4.5(0.3)	2.07(0.09)	0.69(0.05)	0.58(0.05)	7.62(0.01)	0.48(0.02)	5.2
G 173.48+2.45 (0,0)	43.4(0.5)	3.78(0.04)	0.72(0.01)	0.53(0.02)	-16.12(0.01)	2.70(0.03)	49.9
G 173.58+2.44 (0,-20)	12.2(0.4)	1.71(0.06)	0.74(0.04)	0.56(0.05)	-16.42(0.02)	1.63(0.07)	14.0
AFGL 6366 (0,0)	14.7(0.3)	1.56(0.03)	0.70(0.02)	0.56(0.03)	2.68(0.02)	2.16(0.05)	16.9
AFGL 6366 (80,60)	10.5(0.4)	1.45(0.06)	0.67(0.05)	0.53(0.06)	2.10(0.03)	1.63(0.08)	12.0
S 255 (0,60)	27.5(0.6)	2.58(0.05)	0.67(0.02)	0.53(0.03)	8.97(0.02)	2.61(0.06)	31.6
S 76E (-20,-20)	79.3(0.7)	6.03(0.05)	0.70(0.01)	0.53(0.02)	32.44(0.01)	3.10(0.03)	91.1
S 88B (20,20)	4.3(0.8)	0.5(0.2)	0.6(0.4)	0.7(0.4)	22.7(0.1)	1.3(0.4)	5.6
DR 21 (0,-40)	106.3(0.7)	6.93(0.04)	0.72(0.01)	0.66(0.01)	-3.25(0.01)	3.51(0.02)	122.0
S 140 (60,20)	48.2(0.7)	6.53(0.09)	0.64(0.02)	0.56(0.02)	-7.03(0.01)	1.73(0.03)	55.4
L 1251T4 (-60,20)	3.1(0.3)	1.0(0.1)	0.65(0.13)	0.37(0.13)	-3.81(0.03)	0.49(0.05)	3.6
S 153 (0,40)	21.2(1.0)	2.0(0.1)	0.76(0.06)	0.55(0.08)	-51.23(0.05)	2.35(0.12)	24.4
G 264.28+1.48 (20,-20)	6.2(0.1)	0.64(0.01)	0.70(0.02)	0.51(0.02)	6.64(0.01)	2.17(0.04)	7.1
G 265.14+1.45 (0,-60)	15.8(0.2)	1.61(0.02)	0.75(0.01)	0.57(0.02)	7.40(0.01)	2.11(0.03)	18.2
G 267.94-1.06 (0,20)	3.4(0.2)	0.56(0.04)	0.53(0.07)	0.37(0.08)	3.29(0.04)	1.36(0.12)	3.9
G 268.42-0.85 (0,-20)	10.9(0.2)	1.13(0.02)	0.66(0.02)	0.44(0.03)	3.40(0.02)	2.56(0.06)	12.5
G 269.11-1.12 (0,40)	24.3(0.2)	1.66(0.01)	0.76(0.01)	0.56(0.02)	10.49(0.01)	3.23(0.03)	28.0
G 270.26+0.83 (-20,20)	20.9(0.2)	1.44(0.02)	0.73(0.01)	0.49(0.02)	9.69(0.02)	3.42(0.03)	24.0
G 285.26-0.05 (-60,-60)	12.4(0.2)	0.92(0.01)	0.63(0.02)	0.55(0.02)	2.54(0.02)	3.12(0.04)	14.1
G 291.27-0.71 (-80,-100)	36.1(0.2)	2.91(0.01)	0.69(0.01)	0.53(0.01)	-24.36(0.01)	3.00(0.02)	41.6
G 294.97-1.73 (20,-20)	15.6(0.2)	1.53(0.02)	0.69(0.01)	0.41(0.02)	-8.05(0.01)	2.53(0.03)	17.9
G 305.36+0.15 (20,40)	7.0(0.2)	0.47(0.02)	0.69(0.05)	0.64(0.07)	-38.54(0.05)	3.2(0.1)	8.1
G 316.77-0.02 (0,20)	51.6(0.2)	3.53(0.01)	0.72(0.01)	0.60(0.01)	-39.56(0.01)	3.39(0.01)	59.3
G 345.01+1.80 (-20,20)	58.5(0.2)	4.07(0.02)	0.65(0.01)	0.56(0.01)	-14.08(0.01)	3.55(0.01)	67.3
G 345.41-0.94 (80,-20)	13.7(0.2)	1.05(0.01)	0.64(0.01)	0.47(0.02)	-22.31(0.02)	3.25(0.04)	15.7
G 351.41+0.64 (20,100)	128.7(0.2)	6.35(0.03)	0.78(0.01)	0.79(0.01)	-4.23(0.01)	4.38(0.02)	148.0

ample, the $N_2H^+(1-0)$ spectrum toward the peak position in G 351.41+0.64 is shown in Fig. 2 with hyperfine components indicated. The relative amplitudes of the components correspond to the LTE optically thin case. Each component is marked by two pairs of numbers ($F'_1 F' - F_1 F$) corresponding to initial and final states of the transition (Caselli et al. 1995).

After removing baselines from the data (low-order polynomials) we performed gaussian fitting. While choosing three gaussians for fitting the data can give only crude information about position and amplitudes of the components, fitting by seven independent gaussians with fixed separations usually leads to incorrect results (negative amplitudes for some of the overlapped components). We decided to fit the data by seven gaussians, only three of which having independent amplitudes, whereas the amplitudes of the overlapping components have been assumed proportional to their statistical weights. This

method proved to be useful for treating both LTE and non-LTE cases and gave lowest χ^2 values in most cases.

The derived parameters are (Table 3): main beam brightness temperature of the (23-12) component, peak intensity ratios of the (12-12) to (23-12) and (01-12) to (23-12) transitions (R_{12} and R_{02} , respectively), velocity of the (23-12) component and line width at half maximum level, considered equal for all components. For most of the sources the R_{12} ratios do not significantly differ from the optically thin value (5:7) while the R_{02} ratios are usually higher than expected in the optically thin case (3:7). Observed R_{12} versus R_{02} ratios together with the LTE curve are shown in Fig. 3. The mean ratios for the sources given in Table 3 are: $\langle R_{12} \rangle = 0.70(0.01)$ and $\langle R_{02} \rangle = 0.57(0.03)$. Similar ratios apply for each source when all map positions with significant emission are averaged, i.e., $\langle R_{12} \rangle$ is close to 5:7 while $\langle R_{02} \rangle$ is higher than 3:7. Fitting by

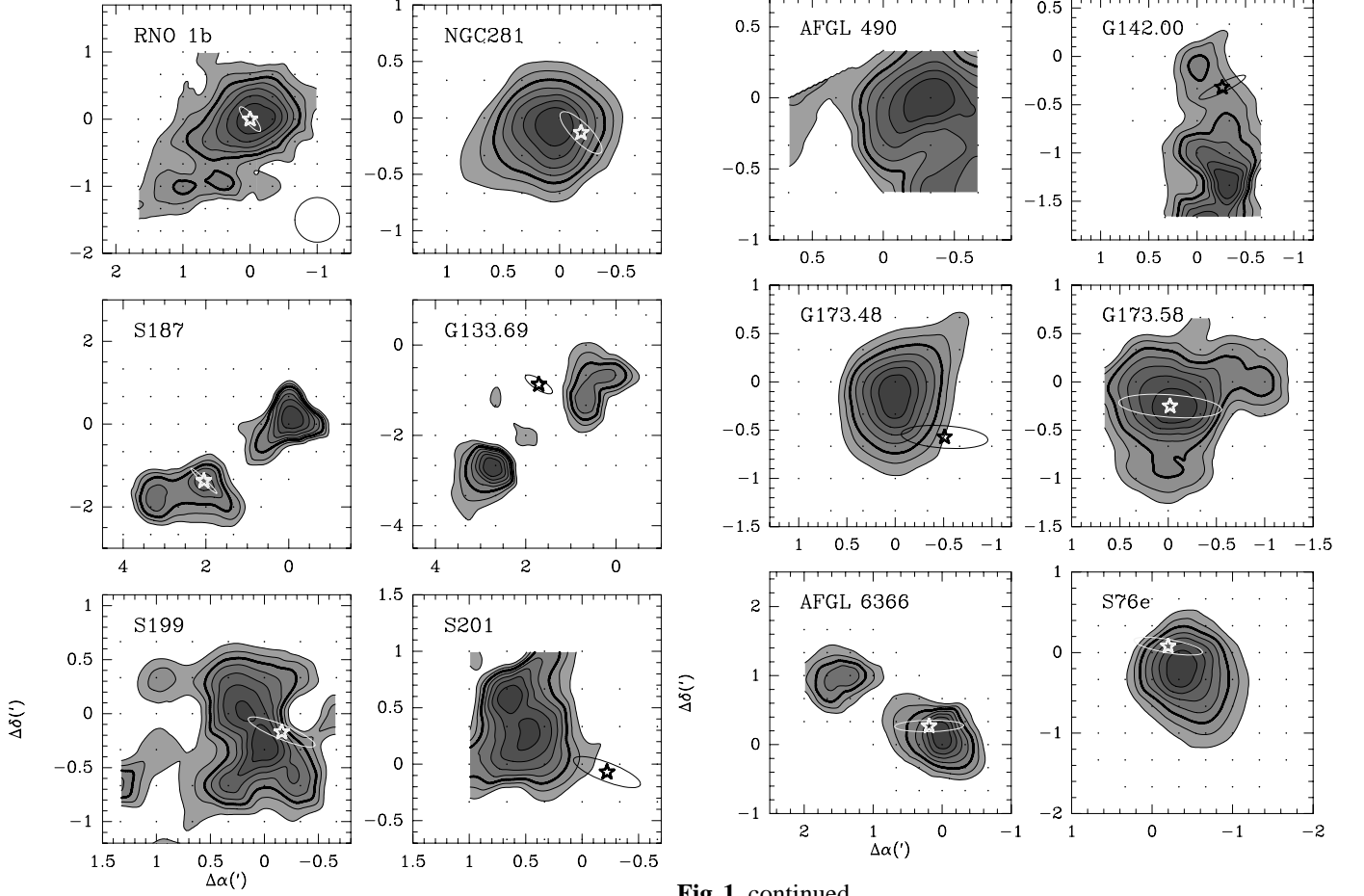


Fig. 1. continued

Fig. 1. $N_2H^+(1-0)$ integrated intensity maps. Intensity contour ranges from 30% to 90% of peak intensity, thick contours correspond to half maximum levels. Observed positions are marked by dots and IRAS point sources are marked by stars. The uncertainty ellipses corresponding to 95% confidence level in IRAS point source position are also shown

three independent gaussians also reveals an enhanced intensity of the (01–12) component compared with the LTE case.

No evidence of broad line wings as indicators of outflow activity has been found in the spectra. The $N_2H^+(1-0)$ spectra towards several positions of G 316.77, G 345.01 and G 351.41 are highly non-gaussian apparently associated with more than one clump along the line of sight. Fitting these spectra by the procedure described above resulted in much higher line widths than for the rest of spectra. No attempts have been made to decompose these spectra into several velocity components due to the ambiguity of such a procedure, and we have excluded these sources from our velocity analysis.

In order to derive line optical depths in the case of closely spaced and overlapping components the following function could be used:

$$T(\nu) = \left[\sum_i J(T_{EX_i}) \frac{\tau_i(\nu)}{\sum_k \tau_k(\nu)} - J(T_{BG}) \right] \cdot \left[1 - \exp\left(-\sum_k \tau_k(\nu)\right) \right], \quad (1)$$

where $J(T) = \frac{h\nu}{k} [\exp(\frac{h\nu}{kT}) - 1]^{-1}$, $T_{BG} = 2.7 K$ is the cosmic background radiation temperature, T_{EX_i} and $\tau_i(\nu)$ are excita-

tion temperature and optical depth of the i -th component at the frequency ν , respectively, and summing is going over all components. For the case of the observed $N_2H^+(1-0)$ spectra the fitting function (1) could be simplified. It is known that excitation temperatures of the overlapping lines always tend to be equal due to photon exchanges (e.g. Guilloteau et al. 1981). Assuming equal excitation temperatures for the overlapping components within triplets, and, that the (01–12) line and the triplets do not overlap, the fitted function becomes:

$$T(\nu) = \left[\sum_i J(T_{EX_i}) - J(T_{BG}) \right] \cdot \left[1 - \exp\left(-\sum_k \tau_{ik}(\nu)\right) \right], \quad (2)$$

where the first sum is going over non-overlapping groups of components and the second is going over overlapping components within individual group. $\tau_{ik}(\nu)$ is the optical depth of the i -th group and k -th overlapping component at the frequency ν . Thus, the fitted parameters are: three excitation temperatures, optical depth of the central (23–12) component as well as line width and velocity of the central component.

The spectra toward the positions given in Table 3 as well as toward several additional emission peaks have been fitted by the function (2). In three sources with low S/N ratios (G 133.69, S 88B and L 1251) the solutions did not converge. In 10 cases the derived optical depth exceeds 3σ . For the remaining sources an upper 3σ level has been derived and it exceeds unity in 8 cases (in the case of S 201 $\tau(23-12) < 3$, the highest upper limit among the sources). The results of fitting for

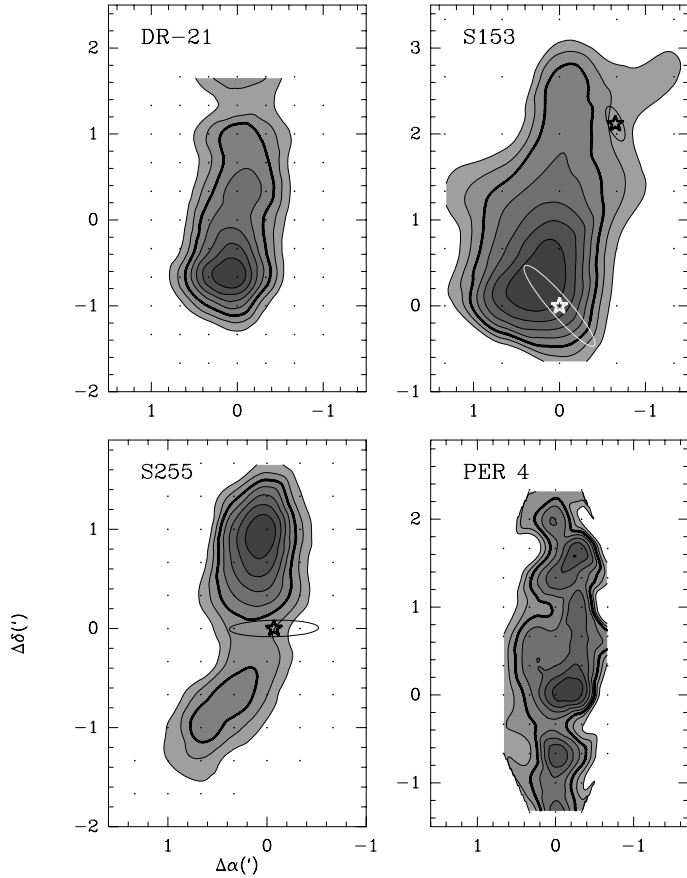


Fig. 1. Continued

10 sources (excitation temperatures, velocities, line widths and optical depths) are given in Table 4. The optical depth and excitation temperature ranges for different sources are: $\sim 0.2-1$ and $\sim 7-29$ K, respectively. The difference in excitation temperature between different groups of components is ≤ 5.6 K and in several cases $T_{EX}(01-12)$ is the highest one. As the sources given in Table 4 are among those with highest intensities we conclude that $T_{EX} \lesssim 25$ K and $\tau(23-12) \lesssim 1$ for the studied sample. It should be emphasized that we have assumed a beam filling factor of 1 in all cases; if smaller, excitation temperatures are higher.

Since non-LTE effects seem small, we have assumed LTE and the optically thin approximation to calculate N_2H^+ column densities, $N(N_2H^+)$, for all sources in Table 3. Excitation temperatures were taken equal to 10 K for all sources, the value at which LTE column densities are close to minimum. At $T_{EX} = 20$ K column densities are 1.6 times higher. The calculated values, which could be treated as lower limits, are given in the last column of Table 3.

3.3. Clump deconvolution

Most of the maps in Fig. 1 show elongated or more complex structures with prominent secondary peaks. In order to estimate core sizes, two-dimensional (2D) gaussian fittings have been used. As a first step we tried to fit simultaneously a number of circular 2D gaussians to each map in order to reveal dis-

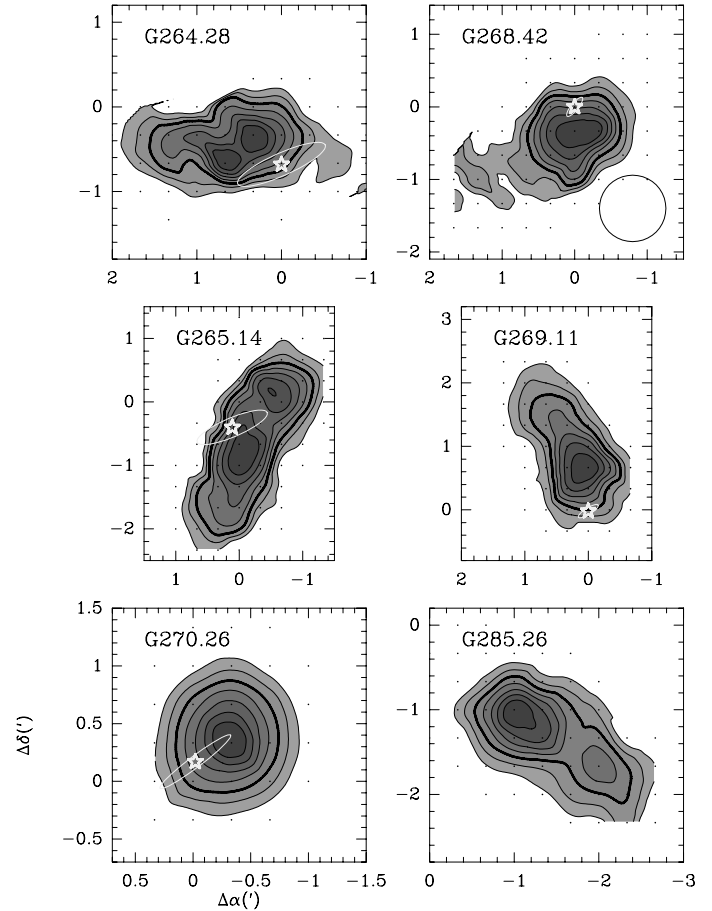
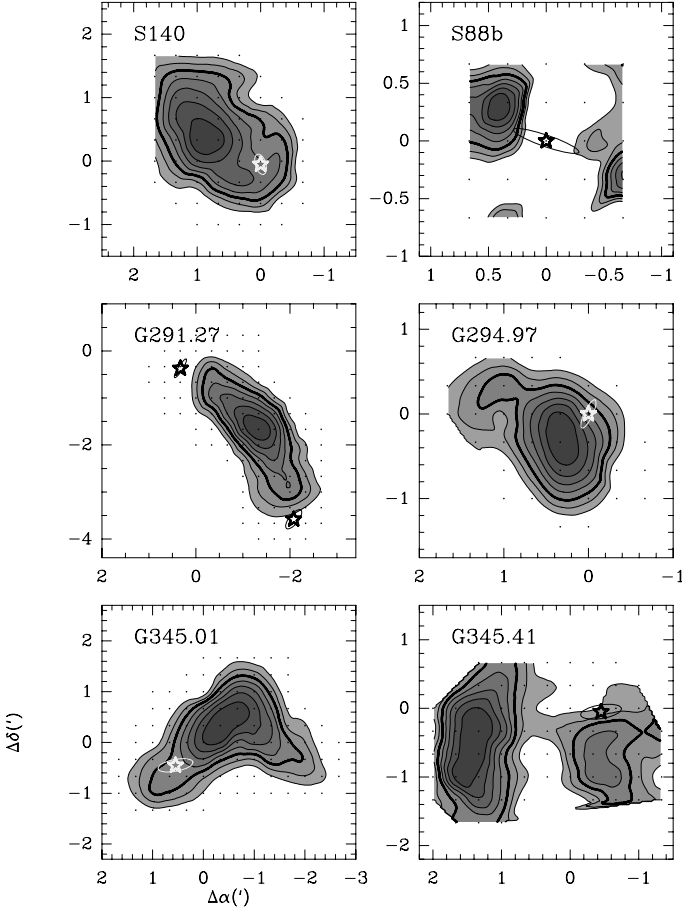


Fig. 1. Continued

tinct clumps. The initial guesses of number of components and their locations were simply based on inspections of the maps in Fig. 1 and strip scans, obtained where required. In the second step the circular gaussians were replaced by elliptical ones, adding two more parameters to be determined: axial ratio and position angle. Finally, core sizes were estimated by deconvolving the geometric mean of the extents of the fitted elliptical gaussians with the beam size, i.e., $C = \sqrt{G^2 - B^2}$ where C , G , and B are the full half widths of the core, observed geometric mean of the extents and beam, respectively. In general, 1–2 clumps per map were found but in several sources (S 187, G 291.27, G 316.77, G 345.01 and G 351.41) three clumps have been revealed. We have excluded Per 4 and L 1251T4 from this analysis, (the former has already been analyzed in Paper I) as well as sources with small (≤ 25 points per map) and incomplete maps. In total, 47 clumps in 26 objects have been revealed. The relative coordinates of the clumps, their axial ratios, angular and linear sizes calculated at half maximum level are given in Table 5 together with fitting uncertainties. We have not taken into account possible uncertainties in source distances while calculating linear sizes. Clumps in the same core are marked by numbers. Angular sizes of some clumps are smaller than the telescope beam. These clumps and those having high uncertainties in size have been excluded from calculations of physical parameters (Section 3.4). For four cores where all revealed clumps are smaller than the telescope beam

Table 4. N₂H⁺(1–0) line parameters with optical depths

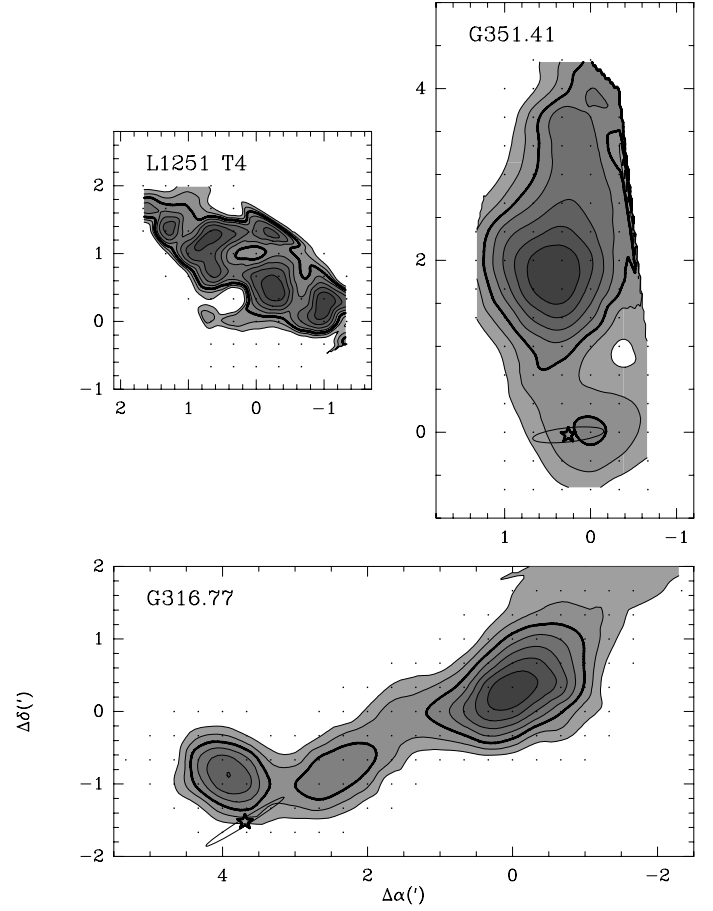
Source ($\Delta\alpha''$, $\Delta\delta''$)	$T_{\text{EX}}(12-12)$ (K)	$T_{\text{EX}}(23-12)$ (K)	$T_{\text{EX}}(01-12)$ (K)	$V_{\text{LSR}}(23-12)$ (km s ⁻¹)	ΔV (km s ⁻¹)	$\tau(23-12)$
RNO 1B (0,0)	7.75(0.37)	9.18(0.38)	7.32(0.50)	-17.54(0.01)	1.94(0.06)	1.0(0.1)
S 255 (0,60)	9.3(1.6)	10.6(1.6)	10.1(2.2)	8.96(0.02)	2.31(0.10)	0.5(0.2)
S 76E (-20,-20)	24.4(4.2)	27.0(4.3)	27.1(5.4)	32.44(0.01)	2.86(0.06)	0.3(0.1)
DR 21 (0,-40)	20.3(1.3)	22.8(1.3)	25.0(2.1)	-3.25(0.01)	3.09(0.04)	0.6(0.1)
S 140 (60,20)	21.4(3.7)	25.4(4.1)	27.0(5.5)	-7.03(0.01)	1.62(0.05)	0.4(0.1)
G 270.26+0.83 (-20,20)	8.8(1.5)	9.2(1.5)	8.8(1.8)	9.69(0.02)	3.17(0.08)	0.3(0.1)
G 291.27-0.71 (-80,-100)	24.2(6.0)	25.9(6.2)	29.1(7.7)	-24.36(0.01)	2.90(0.03)	0.15(0.05)
G 316.77-0.02 (240,-60)	8.9(0.6)	10.1(0.6)	10.1(0.9)	-37.94(0.01)	3.61(0.06)	0.5(0.1)
G 345.01+1.80 (-20,20)	11.8(0.3)	14.3(0.3)	13.4(0.5)	-14.07(0.01)	3.08(0.02)	0.62(0.03)
G 351.41+0.64 (20,100)	16.3(0.3)	18.2(0.2)	20.6(0.5)	-4.20(0.01)	3.65(0.02)	0.86(0.03)

**Fig. 1.** Continued

the parameters of the whole core are also given in Table 5. For three of them (G 265.14, G 269.11 and G 285.26) physical parameters have been calculated.

3.4. Physical parameters of clumps

In column 7 of Table 5 mean line widths averaged over the half maximum intensity regions are given. For overlapping clumps that are not separated at this level, line widths have been aver-

**Fig. 1.** Continued

aged over the whole regions. The following formula was used for weighted averages:

$$\langle \Delta V \rangle = \frac{\sum w_i \Delta V_i}{\sum w_i}, \quad (3)$$

where ΔV_i – velocity dispersion in the i -th position, $w_i = \sigma_i^{-2}$ and σ_i – uncertainty of velocity dispersion in the i -th position

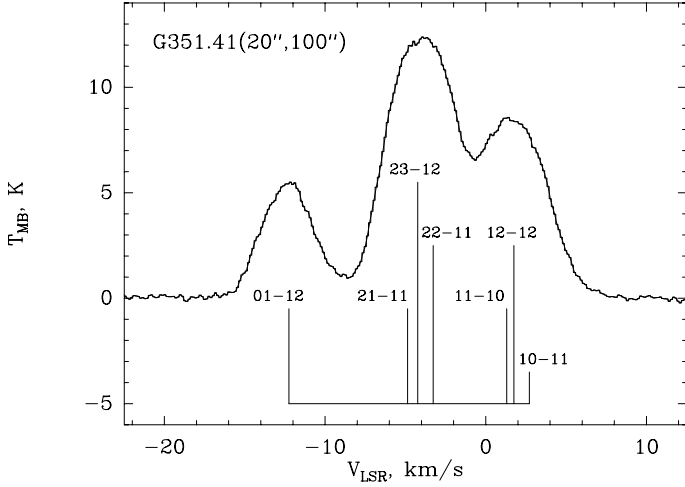


Fig. 2. The $N_2H^+(1-0)$ spectrum toward the intensity peak of G 351.41+0.64. The positions of hyperfine components are indicated. The relative amplitudes of the components correspond to the LTE optically thin case

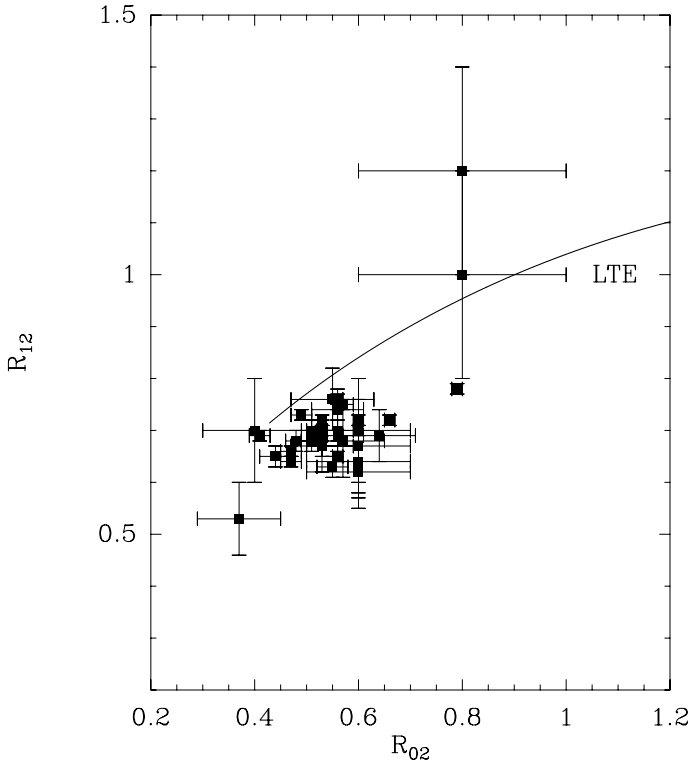


Fig. 3. Ratio of (12–12) to (23–12) peak temperatures versus ratio of (01–12) to (23–12) peak temperatures (R_{12} and R_{02} , respectively). The LTE curve is also shown

calculated from the fit. Uncertainties of mean line width were calculated as:

$$\sigma_{\langle \Delta V \rangle} = \sigma \frac{\sqrt{\sum w_i^2}}{\sum w_i}, \quad (4)$$

where

$$\sigma = \sqrt{\frac{\sum w_i \Delta V_i^2}{\sum w_i} - \langle \Delta V \rangle^2} \quad (5)$$

is the uncertainty of individual line width measurements taking into account point-to-point differences in line widths and using the same weights.

Mean line widths vary from 1 km s^{-1} to 4.7 km s^{-1} , i.e. much higher than thermal widths. So these values should be considered as non-thermal velocity dispersion in the sources without any recalculations.

Following Paper I we have calculated virial masses of homogeneous spherically-symmetrical clumps with no external pressure and no magnetic field (e.g. Pirogov & Zinchenko 1998):

$$M_{\text{vir}}(M_{\odot}) = 105 \langle \Delta V \rangle^2 \cdot d, \quad (6)$$

where ΔV and d are in km s^{-1} and pc units. Virial masses (column 8 of Table 5) lie in the range: $\sim 30 - 3000 M_{\odot}$. These values should be treated as upper limits. If clumps have inner density profiles $\sim r^{-\alpha}$, equation (6) should be multiplied by the factor $\frac{3}{5} \cdot \frac{5-2\alpha}{3-\alpha}$ which for $\alpha \geq 0$ is ≤ 1 . Mean volume densities for spherically-symmetric clumps have been calculated as

$$n_{\text{vir}} = 3M_{\text{vir}} / (4\pi r^3 m), \quad (7)$$

where $r = d/2$ is the radius of the half maximum intensity region, $m = 2.33 \text{ amu}$, mean molecular mass. Mean volume densities lie in the range: $(0.5 - 17.1) \cdot 10^4 \text{ cm}^{-3}$ (see column 9 of Table 5). The N_2H^+ abundances are given in column 10 of Table 5:

$$X(N_2H^+) = \frac{\langle N(N_2H^+) \rangle}{\langle N(H_2) \rangle}, \quad (8)$$

where $\langle N(N_2H^+) \rangle$ is mean column density averaged over the emission region defined by $I/I_{\text{MAX}} \geq 0.5$ and $\langle N(H_2) \rangle$ is molecular hydrogen column density calculated for the same region using virial mass estimate. Calculated abundances lie in the range: $(1.2 - 12.8) \cdot 10^{-10}$. Averaged over 36 analyzed clumps, $\langle X(N_2H^+) \rangle = (5.2 \pm 0.5) \cdot 10^{-10}$.

4. Distributions of the observed parameters over the sources

According to the present theories of star formation radial dependences of density and velocity dispersion (which is considered to be related to magnetic field distribution) are the most important parameters describing the evolution of star forming cores. In particular, the standard theory of low-mass star formation from a singular isothermal sphere (Shu 1977) gives a radial density law $\propto r^{-2}$ for nearly static envelope while in the logatropic sphere model for massive star formation density varies as r^{-1} (McLaughlin & Pudritz 1996). Velocity dispersion in the latter model is nearly constant in the center and rises with distance in the outer regions as $\sim r^{1/3}$.

Recent studies of dust continuum emission in star forming low-mass and massive cores have not revealed significant differences between density power-law indices (α) for these two classes of objects, implying $\alpha \sim 1.5 - 2$. Molecular multi-line modeling of massive cores shows somewhat lower values (see Section 1). An analysis of the $\text{N}_2\text{H}^+(1-0)$ data in low-mass cores (Paper I) revealed the following ranges: $\alpha = 1.8 - 2.8$ for cores with stars, and $\alpha = 1.6 - 1.9$ for cores without stars.

Goodman et al. (1998) found that velocity dispersion profiles in low-mass cores are nearly constant within so-called “coherent regions” with sizes of ~ 0.1 pc, while rising in the outer regions with power-law index ≥ 0.2 which is more in line with the logatropic model. Low-mass cores observed in $\text{N}_2\text{H}^+(1-0)$ (Paper I) imply “coherent lengths” of ~ 0.01 pc but show no common trends in the outer regions. In contrast, molecular line widths in massive cores increase toward the center (Zinchenko 1995, Lapinov et al. 1998, Fontani et al. 2002) which could be connected either with optical depth effects or with an enhancement of dynamical activity of gas in central regions.

In this section we make an attempt to derive N_2H^+ integrated intensity and line width radial profiles on the cores which, under certain assumptions, could be connected with density and velocity dispersion profiles, respectively. An analysis of velocity gradients in the cores which could give a clue to their rotational properties is also given.

4.1. Integrated intensity profiles

As N_2H^+ emission is probably optically thin toward most of the map positions, except peak positions in few of them (see Section 3.2), their integrated intensity distributions should follow column density distributions if excitation conditions do not vary inside the sources. If in addition N_2H^+ abundance is constant, the integrated intensity distribution is directly related to the hydrogen column density distribution. Then, for infinite, spherically-symmetric core the power-law index for volume density profile will be $p + 1$, where p is an integrated intensity power-law index (see e.g. Motte & André 2001).

We performed fitting of $\text{N}_2\text{H}^+(1-0)$ integrated intensity maps for 26 clumps which are not highly elongated (axial ratios < 2) using power-law radial distributions ($\propto r^{-p}$) convolved in 2D with a gaussian telescope beam. Although power laws are not optimal for fitting the radial distributions (e.g. gaussian functions usually give lower χ^2 values) we used them in order to probe different star formation theories. The intensity maps integrated over total line range as well as those integrated over the (01–12) component have been analyzed. The latter should be less affected by optical depth effects than total integrated intensity maps, however, due to lower intensities these maps are more noisy and in several cases fits were not successful. Power-law index, amplitude and coordinates of maximum position have been varied in order to get the best fit. Power-law indices calculated for these two kinds of maps (p and p' , respectively) with fitting uncertainties are given in Table 6. We have also calculated power-law indices for reduced integrated intensity maps which contain only points with intensities equal or higher than 20% and 40% of peak integrated intensity. The

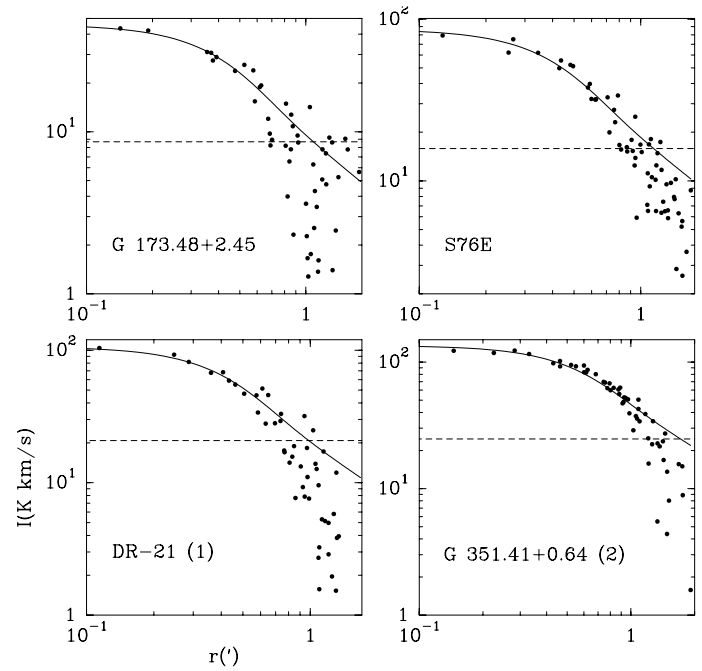


Fig. 4. Four examples of integrated intensity profiles together with the fitted power-law functions convolved with a gaussian telescope beam. The data lower than the dashed lines (20% of peak integrated intensity) were neglected

calculated power-law indices (p_{20} and p_{40} , respectively) and corresponding uncertainties are also given in Table 6. In Fig. 4 four examples of integrated intensity maps as 1D profiles are shown together with fitting results for reduced maps. The radial distance (r) in Fig. 4 is the distance from the maximum of fitting curve to the given point of the map. The data below the dashed lines (20% of peak integrated intensity) have not been taken into account during fitting.

A comparison of the different power-law indices derived for each individual source (Table 6) shows that p and p' are nearly the same confirming the idea that optical depth effects are not important in general. Mean power-law indices averaged over the sources in Table 6 are: $\langle p \rangle = 1.29(0.05)$ and $\langle p' \rangle = 1.34(0.06)$. We have fitted total integrated intensity maps without data points with intensities larger than 90% of the peak, which could mainly suffer from optical depth effects. In this case the power-law indices are also close to p . However, a further comparison of power-law indices calculated for total and reduced maps reveals the following inequality: $p \geq p_{20} \sim p_{40}$ for most of the sources, indicating that $\text{N}_2\text{H}^+(1-0)$ intensity distributions are steeper away from map centers comparing with inner regions and do not follow single power law. Note, that the p_{20} and p_{40} indices calculated over the regions with relatively high intensities could be more influenced by possible saturation effects than the p indices. The effect of steepening of dust intensity distributions in outer regions was found by Beuther et al. (2002) for most of massive star forming cores they studied; they associated this phenomenon with finite sizes of the cores. $\text{N}_2\text{H}^+(1-0)$ integrated intensity profiles in low mass cores also demonstrated the same effect (Paper I) but it was explained by fast drop in excitation temperature caused

Table 6. Power-law indices calculated from fits of power-law distributions convolved with the telescope beam to $N_2H^+(1-0)$ integrated intensity maps with axial ratios < 2

Source	p	p'	p_{20}	p_{40}
RNO 1B	0.91(0.05)	0.89(0.09)	0.83(0.05)	0.68(0.09)
NGC 281	1.42(0.06)	1.34(0.16)	1.17(0.08)	1.19(0.02)
S 187 (1)		0.83(0.21)	0.79(0.05)	0.94(0.09)
S 187 (3)	1.19(0.22)		0.82(0.14)	0.76(0.09)
G 133.69+1.22 (1)	0.91(0.20)		1.37(0.10)	
S 199	0.96(0.11)		0.74(0.11)	0.39(0.28)
S 201	1.30(0.15)		1.02(0.20)	0.67(0.29)
G 173.48+2.45	1.31(0.04)	1.40(0.05)	1.08(0.06)	0.98(0.08)
G 173.58+2.44	1.07(0.08)	0.97(0.26)	0.84(0.07)	0.70(0.10)
AFGL 6366 (1)	1.48(0.03)	1.20(0.25)	1.14(0.01)	1.27(0.26)
AFGL 6366 (2)	1.43(0.11)	1.13(0.20)	1.25(0.08)	1.21(0.37)
S 76E	1.22(0.03)	1.13(0.04)	1.06(0.05)	0.93(0.07)
DR 21 (1)	1.42(0.03)	1.47(0.03)	1.12(0.09)	1.04(0.09)
DR 21 (2)	1.15(0.08)	1.14(0.09)	0.78(0.12)	0.51(0.20)
S 140 (1)	0.99(0.05)	1.02(0.08)	0.81(0.05)	0.65(0.08)
S 140 (2)	1.19(0.06)	1.11(0.10)	0.80(0.13)	0.54(0.14)
S 153 (1)	1.29(0.14)	1.30(0.32)	1.12(0.09)	
S 153 (2)	1.08(0.11)	1.23(0.25)	0.66(0.08)	0.46(0.08)
G 268.42-0.85	1.35(0.10)	1.58(0.26)	0.97(0.13)	0.72(0.31)
G 291.27-0.71 (1)	1.33(0.06)	1.41(0.10)	1.05(0.05)	0.94(0.08)
G 345.01+1.80 (1)	1.35(0.03)		0.99(0.10)	0.69(0.15)
G 345.01+1.80 (2)	1.37(0.03)	1.40(0.04)	1.05(0.06)	0.76(0.09)
G 345.41-0.94 (2)	0.75(0.09)	0.89(0.17)	0.72(0.08)	0.63(0.05)
G 351.41+0.64 (1)	1.40(0.08)	1.41(0.03)	1.01(0.01)	0.77(0.04)
G 351.41+0.64 (2)	1.30(0.02)	1.36(0.05)	1.01(0.03)	0.90(0.04)
G 351.41+0.64 (3)	1.24(0.05)	1.34(0.08)	0.90(0.08)	0.77(0.11)

by density drop in outer core regions. The latter seems doubtful since the same cores mapped in CS are usually more extended than in N_2H^+ (Zinchenko et al. 1994, 1995, 1998; Juvela 1996), instead, the fast decrease of intensities could be caused by N_2H^+ abundance drop (A. Lapinov, private communication).

Mean power-law indices for reduced maps averaged over the sources in Table 6 are: $\langle p_{20} \rangle = 1.05(0.06)$ and $\langle p_{40} \rangle = 0.96(0.10)$. Assuming excitation conditions are constant and saturation effects are small in the interior regions where $I/I_{MAX} \geq 0.2$, the derived power-law indices more likely correspond to density profiles $\propto r^{-2}$ as the theory of isothermal sphere predicts (Shu 1977). This is in general consistent with mean power-law index 1.6(0.5) found by Beuther et al. (2002) for radial density profiles in inner clump regions ($\leq 32''$) of massive star forming cores as well as with the value 1.8(0.4) derived by Mueller et al. (2002) for dense cores associated with water masers. Our sample includes seven sources explored by Mueller et al. (2002), and for five of them (RNO 1B, NGC 281, G 173.48, S 76E and S 140) we have got intensity profile power-law indices. However, density power-law indices derived by Mueller et al. (2002) are systematically lower by $\sim 0.4 - 0.6$ than the values $p_{20} + 1$ expected for density profiles from our data for inner clump regions. Model calculations of N_2H^+ excitation in dense cores as well as maps of optically thin dust emission for the rest of our core sample are highly desirable to explain the origin of the discrepancy.

4.2. Velocity dispersion profiles

The values of line widths obtained from spectra fits are much larger than thermal widths (kinetic, dust or peak CO(1-0) temperatures for the sample sources are $\sim 20 - 50$ K, see Schreyer et al. 1996, Zinchenko et al. 1995, 1997, 1998) and could be

used as a measure for dispersion of non-thermal velocities in the sources. This parameter is widely used in theoretical models describing non-thermal motions of gas within dense cores and is important for calculations of equation of state, stability and evolution of dense envelopes around newborn stars.

We have compared line width and integrated intensity maps and found that in most cases the shapes of the regions with constant line width do not follow directly integrated intensity distributions demonstrating more complex clumpy structures.

Since one-dimensional line width profiles demonstrate large scatter, we used the method from Paper I to calculate a dependence of averaged line widths on impact parameters. Only the values higher than 3σ were taken for averaging. Here, the impact parameter (b) is the square root of A/π , where A is the area of the region enclosing all the points with intensity larger than certain level, which in turn varies from I_{max} to $0.05 \cdot I_{max}$ with a step $0.01 \cdot I_{max}$. If the difference $b_i - b_{i-1}$ becomes higher than half of the mapping step ($10''$) the averaged line width and its uncertainty have been calculated for this region according to the formulas (3–5).

In Fig. 5 velocity dispersion profiles are given for ten sources having at least 5 points per profile including seven cores with one clump and three clumps separated from their neighbours at half maximum intensity level. The number of averaged values per point on the plots increases with b from 1 to 10–15 at the edge. Uncertainties of averaged line widths also increase with b (if they are lower than $(\sum \sigma_i^{-2})^{-1/2}$, where σ_i is the line width uncertainty in the i -th map position calculated from the spectral fit, the latter values are shown). The cores with one clump demonstrate that velocity dispersion decreases with impact parameter or remains nearly constant in one case (NGC 281). In 5 of these 7 cases, IRAS sources (taking into account their position uncertainties) are located within 90% of peak intensity level. In the three remaining clumps in Fig. 5 there is no clear $\Delta V - b$ trend and either no associated IRAS source or it is located outside half maximum intensity level. RNO 1B, S 199 and G 268.42 demonstrate the steepest slopes. Differences between central line widths and those at the edges of these cores are $\sim 1 - 1.5$ km s $^{-1}$. For eight cores with more than one clump per core and at least 5 points per profile which are not shown in Fig. 5 there is a decrease of line width with impact parameter at least in two cases, G 269.11 and G 264.28. In other cases no clear trend has been found.

An enhancement of line width in central regions in several cases could be at least in part due to optical depth effects. In fact, line optical depths $\sim 0.5 - 1.5$ can result in $\sim 1.1 - 1.3$ gaussian line broadening due to saturation (e.g. Phillips et al. 1979). Therefore, the line width profiles in RNO 1B, S 76E (optical depths are given in Table 4) and, probably, in S 199, G 173.48 and G 173.58, where optical depths are more uncertain (1.3 ± 0.7 , 0.2 ± 0.1 and 0.6 ± 0.3 , respectively), could partially suffer from this effect but cannot alone explain the observed trends in all the cases. The conclusion will not change if the objects consist of small unresolved clumps.

A plausible explanation could be found in a larger degree of dynamical activity of gas in central regions in the vicinity of IRAS point sources, including differential rotation, infall mo-

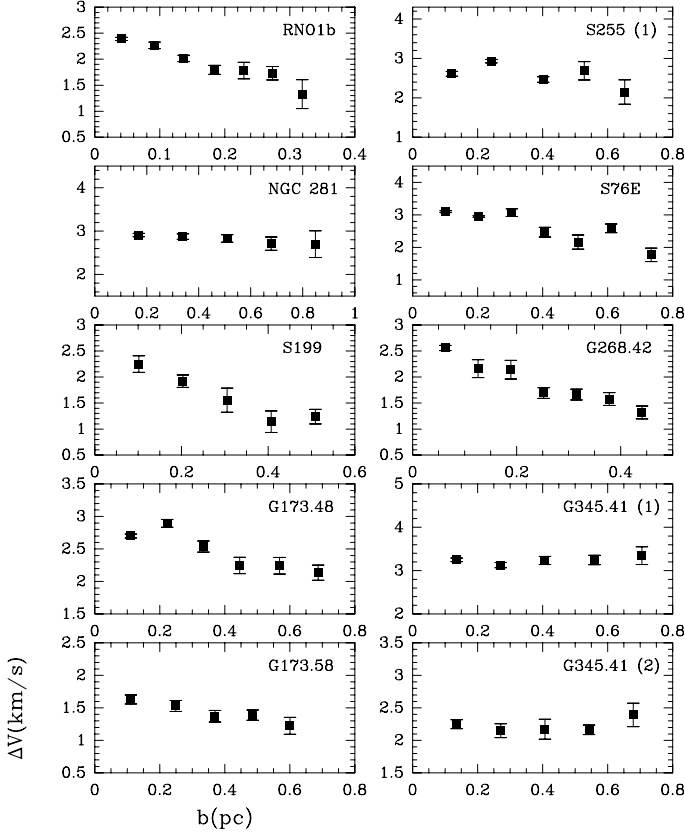


Fig. 5. Radial velocity dispersion profiles for the cores with one clump and clumps separated at half maximum intensity level

tions and turbulence due to winds and outflows from massive stars.

4.3. Velocity gradients

It is known that an analysis of spatial distributions of line-of-sight velocities is fruitful in revealing rotational motions of gas (Goodman et al. 1993). In particular, solid body rotation should produce linear gradients on V_{LSR} maps. Velocity gradients also have been interpreted in terms of turbulent motions by Burkert & Bodenheimer (2000).

In order to investigate velocity structure of the sample cores we have used a least squares fitting program (Goodman et al. 1993, Paper I) which calculates local and total linear velocity gradients for a given core (see Paper I for a detailed explanation of the program). The results of fits are summarized in Table 7 where the magnitude (Γ) and the direction (Θ_{Γ} , direction of increasing velocity, measured east of north) of the total velocity gradient in each core, the product of the velocity gradient and core size ($\Gamma \times d$), and β , the ratio of rotational to gravitational energy (Goodman et al. 1993, Paper I) are given. We have not separated all the cores into clumps (as has been done in Section 4.1) except those having clumps that do not overlap at half maximum intensity level (S 187, G 133.69, AFGL 6366, S 255 and G 345.41).

In Fig. 6 local velocity gradient maps (white arrows) overlaid over integrated intensity maps (grey scaled) are shown

Table 7. Results of gradient fitting

Source	Γ (km s ⁻¹ pc ⁻¹)	Θ_{Γ} (deg E of N)	$\Gamma \times d$ (km s ⁻¹)	β (10 ⁻³)
RNO 1B	1.64(0.04)	145.8(1.1)	0.8	11.6
NGC 281	0.42(0.03)	-59.3(3.5)	0.3	1.5
S 187 (1)	1.10(0.11)	11.0(6.1)	0.3	16.1
S 187 (2+3)	1.47(0.13)	-135.1(4.9)	0.7	28.5
G 133.69+1.22 (1)	2.90(0.25)	141.9(5.3)	2.3	67.8
G 133.69+1.22 (2)	0.48(0.09)	-75.4(5.0)	0.2	2.4
S 199	0.27(0.03)	-24.4(7.4)	0.2	3.6
S 201	1.35(0.11)	143.9(4.0)	0.6	20.0
G 173.48+2.45	1.25(0.01)	26.1(0.8)	0.8	12.1
G 173.58+2.44	0.47(0.03)	149.4(3.1)	0.4	10.8
AFGL 6366 (1)	0.28(0.05)	-89.5(13.3)	0.1	0.4
AFGL 6366 (2)	0.99(0.06)	-120.2(3.4)	0.5	10.6
S 255 (1)	1.39(0.03)	-28.9(1.9)	0.8	13.7
S 255 (2)	0.59(0.03)	-35.1(3.4)	0.4	7.4
S 76E	0.52(0.01)	-175.9(1.6)	0.4	2.3
DR 21	0.41(0.01)	-95.8(0.4)	0.5	3.9
S 140	0.41(0.02)	58.6(2.5)	0.2	1.4
S 153	0.09(0.02)	-122.8(9.5)	0.2	1.0
G 264.28+1.48	1.15(0.03)	108.7(2.3)	0.3	3.0
G 265.14+1.45	0.82(0.01)	-69.5(0.6)	0.5	7.0
G 268.42-0.85	0.92(0.03)	122.7(1.9)	0.3	8.3
G 269.11-1.12	0.66(0.01)	-88.4(0.5)	0.6	7.6
G 285.26-0.05	0.46(0.01)	-123.7(1.3)	0.7	7.2
G 291.27-0.71	0.158(0.004)	113.3(1.2)	0.2	0.6
G 294.97-1.73	1.33(0.03)	-112.4(1.2)	0.5	5.1
G 345.41-0.94 (1)	0.81(0.01)	-176.6(1.4)	0.9	10.7
G 345.41-0.94 (2)	1.05(0.02)	-87.3(0.8)	1.6	70.8

for 20 cores. Two objects (S 187 and G 133.69) are not shown due to small number of points per local gradient map. The arrows point towards increasing V_{LSR} . Total velocity gradients calculated for the whole cores or distinct clumps are shown by bold arrows; their values are also indicated. Many sources show systematic and at least in some parts of maps nearly constant (both in magnitude and direction) velocity gradient fields, implying nearly uniform rotation (e.g. RNO 1B, S 201, G 173.48, G 173.58, S 255, G 264.28, G 265.14).

The cores with (not separated) closely located clumps usually have more complex velocity fields than those composed of single clump or more clumps separated at the half maximum intensity level. No direct link between velocity gradient distribution and IRAS source location has been found. The direction of constant velocity gradient field in several cases is close to elongation angle of the core. For 17 cores resolved in both directions there is a correlation between direction angle of total velocity gradient (Θ_{Γ}) and elongation angle found from 2D gaussian fitting of integrated intensity maps, with correlation coefficient, $cc = 0.9$. This fact satisfies an assumption that elongation of cores and clumps could be due to rotation. Yet, β values vary from $4 \cdot 10^{-4}$ to $7.1 \cdot 10^{-2}$ with the mean value of 0.01 for 27 sources (Table 7, last column). These ratios are the lowest ones among dense cores with 0.2–2 pc sizes (Phillips 1999). Thus, rotation should not play significant role in core dynamics.

5. Correlations between mean velocity dispersions, column densities and sizes

We have searched for possible correlations between mean line widths (or mean non-thermal velocity dispersions) and emission region sizes for the cores and clumps found by deconvolution method (see Section 3.3). Beginning from the works of

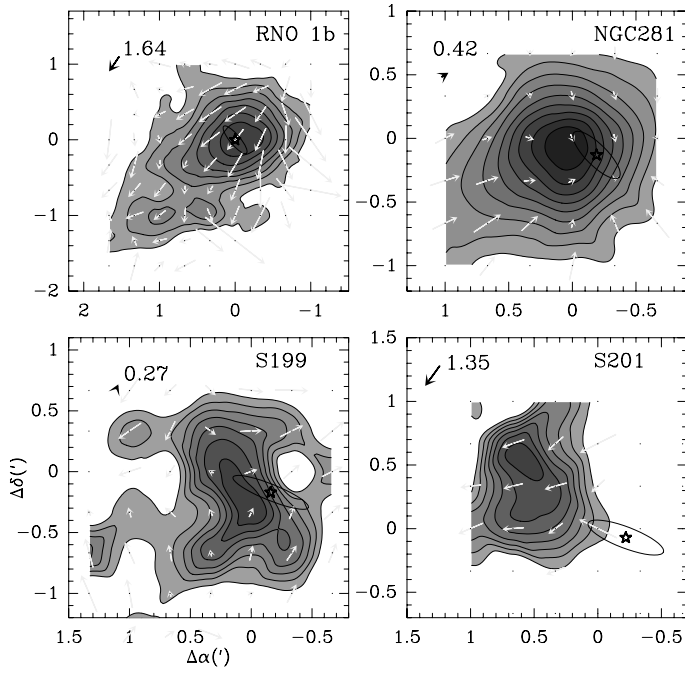


Fig. 6. Local velocity gradient maps superposed on integrated intensity maps. Total velocity gradients are shown by bold arrows together with their values (in $\text{km s}^{-1} \text{pc}^{-1}$). IRAS point sources are marked by stars. The uncertainty ellipses are also shown

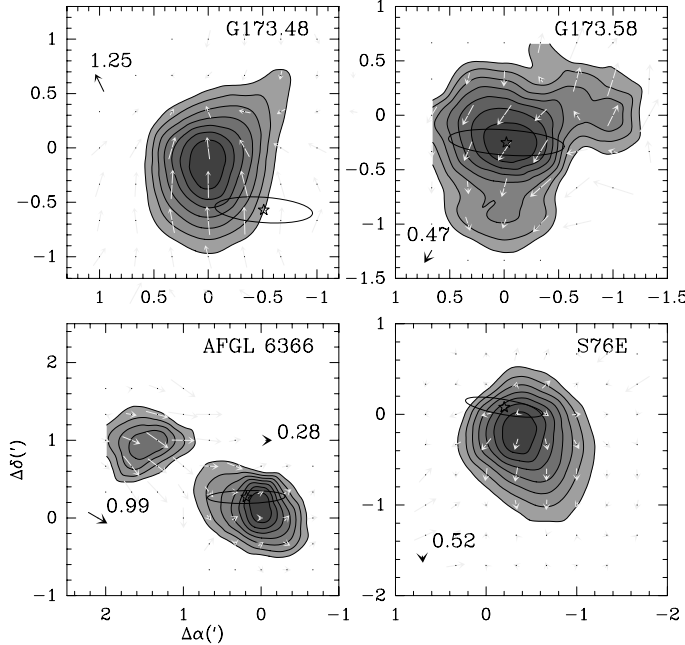


Fig. 6. Continued

Larson (1981) and Myers (1985) such correlations are widely used in estimates of clouds stability and turbulence.

In Fig. 7(a) we plot mean line widths versus emission region sizes in logarithmic scale for 26 cores and clumps having size estimates (Table 5), with the exception of three cores presenting more than one velocity component (G 316.77, G 345.01 and G 351.41). The correlation coefficient between param-

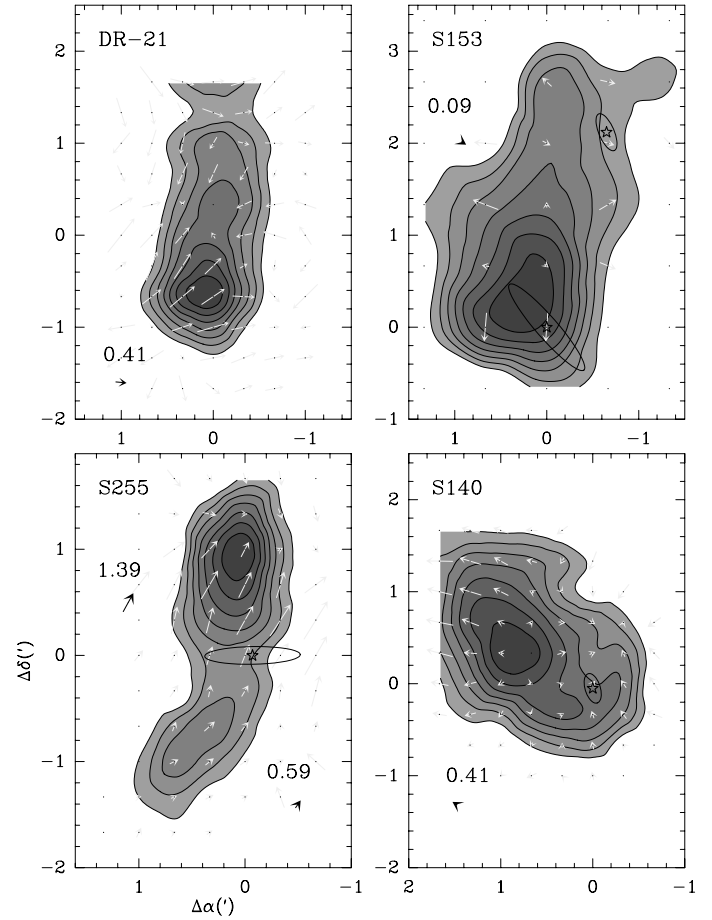


Fig. 6. Continued

eters is not high (~ 0.5), yet, the correlation is significant. The hypothesis of zero correlation is rejected at 0.6% significance level (Press et al. 1992). The slope of the regression line, calculated by the ordinary least-squares method, is $0.3(0.1)$, and the intercept coefficient is $0.38(0.03)$. Practically, the same results have been obtained excluding the cores with steepest line width profiles (RNO 1B, S 199 and G 268.42, see Section 4.2), for which mean line widths could be enhanced due to additional broadening in the central regions of the maps. However, since the compared variables are independent, it could be more correct to use linear regression methods that treat them symmetrically (e.g. orthogonal, reduced major-axis or bisector methods, see Isobe et al. 1990). Applying these methods to the data we have obtained higher slopes ($0.4-0.65$) and nearly the same intercept values.

The regression line calculated by the ordinary least-squares method is shown in Fig. 7(a) as a solid line together with two additional linear regressions found by other authors with the same method for massive cores. Whereas the dependence of Caselli & Myers (1995) (dashed line) was calculated using multi-line data for more compact cores in Orion A and B, the dependence of Zinchenko (2000) (dotted line) was calculated for the sample observed in CS and $C^{34}S$. All the slopes agree within the uncertainties of their determination.

We have also searched for possible correlations between peak N_2H^+ column densities (which in the case of con-

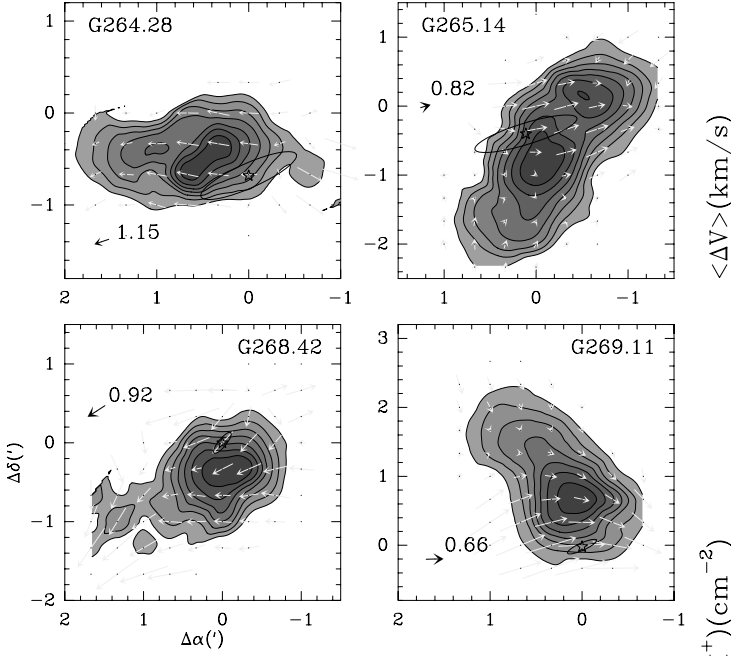


Fig. 6. Continued

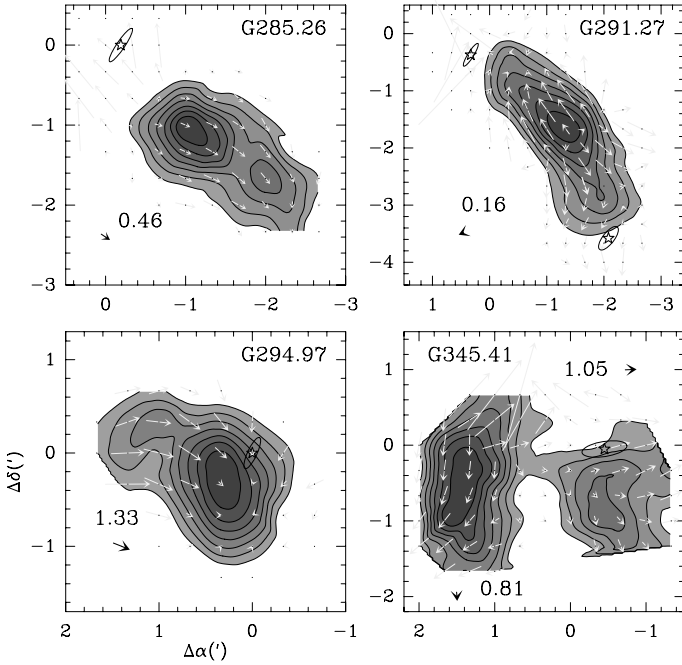


Fig. 6. Continued

stant N_2H^+ abundances trace hydrogen column densities) and sizes (Fig. 7(b)). These parameters have been chosen because they are independent, unlike to mean densities and virial masses which have been calculated using size estimates (see Section 3.4). No significant correlation has been found. No correlation has been also found between mean N_2H^+ column densities (averaged over emission regions with $I/I_{MAX} \geq 0.5$) and sizes.

It is doubtful that the observed $\langle \Delta V \rangle - d$ dependence is connected with general turbulence properties or with some common equation of state for the sample cores. As it is shown

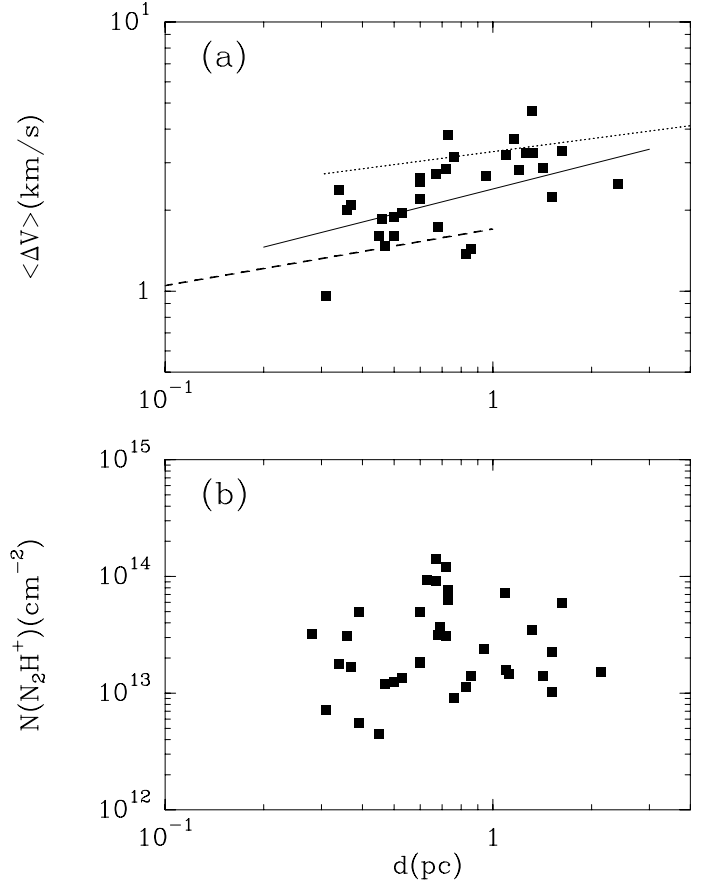


Fig. 7. Mean line widths versus emission region sizes (a) together with regression (solid) line. Dashed and dotted lines correspond to the line width – size relations from Caselli & Myers (1995) and Zinchenko (2000), respectively. Peak N_2H^+ column densities versus emission region sizes (b)

in Section 4.2 there is no evidence for growing line width with distance inside the cores. On the other hand, the dependence found does not contradict the assumption of gravitationally bounded objects in virial equilibrium. Depending on the so-called virial parameter, M_{vir}/M (Bertoldi & McKee 1992), where virial mass is calculated from equation (6) and M is an independent estimate of mass, such objects could be in the critical state on the threshold of gravitational collapse ($M_{vir}/M \sim 1$) or in pressure equilibrium ($M_{vir}/M \gg 1$) (e.g. Pirogov & Zinchenko 1998). If the cores are close to the critical state, with magnetic energy being of the order of kinetic energy, the slope of the $\langle \Delta V \rangle - d$ dependence should be equal to 0.5, with intercept coefficient depending on external pressure and inner density profile. Column density in this case does not depend on size. If the cores are in pressure equilibrium, any $\langle \Delta V \rangle \propto d^q$ dependence implies a corresponding $M \propto d^{3-2q}$ dependence.

Our virial masses for four cores coincide within a factor of 1.5 with the M_n masses found by Mueller et al. (2002), and in one case (RNO 1B) the virial mass is ~ 5 times lower than the corresponding M_n value, which could be connected with differences in core size. Masses derived from CS observations for most of the sample sources (Zinchenko et al. 1994, 1995, 1998;

Juvela 1996) are several times larger than our virial masses (except G 316.77), yet, CS emission is usually more extended. Therefore, if the studied cores are in equilibrium, they could be close to the critical state rather than in pressure equilibrium.

6. Comparison with physical parameters of low-mass cores

In Table 8 physical parameters of the clumps averaged over the studied sample are given together with the same parameters derived in Paper I for low-mass cores with and without stars. Physical parameters for massive cores are taken from Table 3 and Table 5. We have used weighted averages for the parameters which uncertainties resulted from fits (line width, size, axial ratio, power-law index, velocity gradient), for the others standard arithmetic means are given. In brackets we give standard deviations (as in Paper I).

Apart from well-known differences in virial mass and velocity dispersion between these two samples, one can see that massive cores have higher sizes and column densities, lower mean densities and velocity gradients than low-mass counterparts. Note, that for low-mass cores $d = 2r$, where r was taken from Table 6 of Paper I. Mean power-law indices for integrated intensity maps for the studied cores are also given as well as the same parameters for low-mass cores (see Table 6 from Paper I, $p = \alpha - 1$). On average, integrated intensity profiles in massive cores have nearly the same power-law indices as in low-mass cores within uncertainties of their determination. Mean axial and β ratios, as well as mean N_2H^+ abundances also are nearly the same taking into account their uncertainties. Velocity dispersion in massive cores is either constant or decreases with distance from the center in contrast to low-mass cores where no common tendency was found.

The fact that mean density in massive cores is lower than in low-mass cores is somewhat unexpected. For example, Fontani et al. (2002) recently found densities of $10^5 - 10^6 \text{ cm}^{-3}$ for the sample of massive cores associated with ultracompact H II regions and having sizes 0.2–1.6 pc. Possible explanation could be found if dense cores from our sample actually consist of unresolved clumps much smaller than the telescope beam. If density of such unresolved clumps is the same as for low-mass cores with stars (see Table 8) the clumps volume filling factor should be ~ 0.3 .

7. Conclusions

In order to derive physical conditions of dense gas in molecular cloud cores where massive stars and star clusters are formed, 35 objects from northern and southern hemispheres have been observed in the $N_2H^+(1-0)$ line. N_2H^+ emission has been detected in 33 sources, and detailed maps have been obtained for 28 sources. The results can be summarized as follows:

1. Peak LTE N_2H^+ column densities lie in the range: $3.6 \cdot 10^{12} - 1.5 \cdot 10^{14} \text{ cm}^{-2}$. Intensity ratios of (01–12) to (23–12) hyperfine components in most cases are slightly higher than the LTE value. The optical depth of (23–12) component toward peak intensity positions of 10 sources is $\sim 0.2 - 1$.

2. N_2H^+ intensity maps in most cases show elongated or more complex structures. Two-dimensional gaussian fittings have revealed 47 clumps in 26 objects. Their sizes lie in the range: 0.3–2.1 pc, the range of virial masses is $\sim 30 - 3000 M_\odot$. Mean N_2H^+ abundance for 36 clumps is $(5.2 \pm 0.5) \cdot 10^{-10}$.
3. Power-law indices for radial integrated intensity profiles in the cores with axial ratios < 2 have been calculated. The mean value of power-law index is close to 1.3 for total integrated intensity maps in 25 objects, and about unity for reduced maps, where positions of low intensity were rejected. This corresponds to a density profile $\propto r^{-2}$ in the core inner regions, assuming constant N_2H^+ excitation conditions and abundances, and small saturation effects.
4. In the cores with relatively extensive and high quality maps N_2H^+ line widths either decrease or stay constant with distance from the center implying an enhanced dynamical activity in the central regions in the vicinity of IRAS sources.
5. Elongation angles of the 17 cores and distinct clumps correlate with total velocity gradient direction confirming that elongation could be due to rotation. However, the ratio of rotational to gravitational energy ($4 \cdot 10^{-4} - 7.1 \cdot 10^{-2}$) is too low for rotation to play a significant role in the dynamics of the cores.
6. A correlation has been found between mean line widths and sizes of the clumps, $\langle \Delta V \rangle \propto d^{0.3 \pm 0.1}$. No correlation has been found between peak N_2H^+ column densities and the sizes. These results do not contradict the assumption of gravitationally bounded objects in virial equilibrium.
7. A comparison between mean physical parameters of massive and low-mass cores (Paper I) reveals that massive cores have higher sizes, N_2H^+ column densities, virial masses and velocity dispersions as well as lower mean densities and velocity gradients than low-mass counterparts. Mean N_2H^+ abundances, axial ratios and ratios of rotational to gravitational energy are nearly the same. N_2H^+ integrated intensity profiles have nearly the same mean power-law indices while velocity dispersions in massive cores have a tendency to decrease with distance in contrast to low-mass cores, where no common trend was found.

Acknowledgements. We are grateful to A. Lapinov for valuable comments. We would like to thank the anonymous referee for useful detailed comments. The research has made use of the SIMBAD database, operated by CDS, Strasbourg, France. The work was supported by NASA-CRDF grant RPO-841, INTAS grant 99-1667 and Russian Foundation for Basic Research grant 03-02-16307 (in part). PC wish to acknowledge support from the MURST project ‘‘Dust and molecules in astrophysical environments’’. PCM would like to acknowledge NASA grant NAG-6266.

References

- Bergin, E. A., Snell, R. L., & Goldsmith, P. F., 1996, ApJ, 460, 343
 Bertoldi, F., & McKee, C. F., 1992, ApJ, 395, 140
 Beuther, H., Schilke, P., Menten, K. M., Motte, F., Sridharan, T. K., & Wyrowski, F., 2002, ApJ, 566, 945
 Blitz, L., Fich, M., & Stark, A. A., 1982, ApJS, 49, 183
 Brand, J., & Blitz, L., 1993, A&A, 275, 67

- Burkert, A., & Bodenheimer, P., 2000, *ApJ*, 543, 822
- Carpenter, J. M., Snell, R. L., Schloerb, F. P., & Skrutskie, M. F., 1993, *ApJ*, 407, 657
- Caselli, P., Myers, P. C., & Thaddeus, P., 1995, *ApJ*, 455, L77
- Caselli, P., & Myers, P. C., 1995, *ApJ*, 446, 665
- Caselli, P., Benson, P. J., Myers, P. C., & Tafalla, M., 2002, *ApJ*, 572, 238 (Paper I)
- Fich, M., & Blitz, L., 1984, *ApJ*, 279, 125
- Fontani, F., Cesaroni, R., Caselli, P., & Olmi, L., 2002, *A&A*, 389, 603
- Goodman, A. A., Benson, P. J., Fuller, G. A., & Myers, P. C., 1993, *ApJ*, 406, 528
- Goodman, A. A., Barranco, J. A., Wilner, D. J., & Heyer, M. H., 1998, *ApJ*, 504, 223
- Guilloteau, S., Lucas, R., & Omont, A., 1981, *A&A*, 97, 347
- Harvey, P. M., Campbell, M. F., & Hoffmann, W. F., 1977, *ApJ*, 211, 786
- Harvey, P. M., Campbell, M. F., Hoffmann, W. F., & Thronson Jr., H. A., 1979, *ApJ*, 229, 990
- Harvey, P. M., Joy, M., Lester, D. F., & Wilking, B., 1986, *ApJ*, 300, 737
- Hodapp, K.-W., 1994, *ApJS*, 94, 615
- Isobe, T., Feigelson, E. D., Akritas, M. G., & Babu G. J., 1990, *ApJ*, 364, 104
- Jijina, J., Myers, P. C., & Adams, F. C., 1999, *ApJS* 125, 161
- Juvela, M., 1996, *A&AS*, 118, 191
- Lada, C. J., 1985, *ARA&A*, 23, 267
- Lapinov, A. V., Schilke, P., Juvela, M., & Zinchenko I. I., 1998, *A&A*, 336, 1007
- Larson, R. B., 1981, *MNRAS*, 194, 809
- Martin, K., & Henning, Th., 1992. In: Klare G. (ed.) *Stellar Evolution and Interstellar Matter* (Astronomische Gesellschaft, Abstract Series No. 7). Colordruck Kurt Weber, Hamburg, 77.
- Motte, F., & André, P., 2001, *A&A*, 365, 440
- McLaughlin, D. E., & Pudritz, R. E., 1996, *ApJ*, 469, 194
- McLaughlin, D. E., & Pudritz, R. E., 1997, *ApJ*, 476, 750
- Mueller, K. E., Shirley, Y. L., Evans II, N. J., & Jacobson, H. R., 2002, *ApJS*, 143, 469
- Myers, P. C. In: *Protostars and Planets II* (eds Black D. C. and Matthews M. S.). Univ. Arizona Press, Tucson, 1985, 81
- Neckel, T., 1978, *A&A*, 69, 51.
- Plume, R., Jaffe, D. T., & Evans II, N. J., 1992, *ApJS*, 78, 505
- Phillips, J. P., 1999, *A&AS*, 134, 241
- Phillips, T. G., Huggins, P. J., Wannier, P. G., & Scoville, N. Z., 1979, *ApJ*, 231, 720
- Pirogov, L., 1999, *A&A*, 348, 600
- Pirogov, L. E., & Zinchenko, I. I. 1998, *AZh*, 75, 14 (*Astron. Rep.*, 42, 11)
- Press, W. H., Teukolsky, S. A., Vetterling, W. T., & Flannery B. P., 1992, *Numerical Recipes in Fortran 77*, Cambridge Univ. Press
- Schreyer, K., Henning, Th., Kömpe, C., & Harjunpää, P. 1996, *A&A*, 306, 267
- Shirley, Y. L., Evans II, N. J., & Rawlings, J. M. C., 2002, *ApJ*, 575, 337
- Shu, F. H., 1977, *ApJ*, 214, 488
- Snell, R. L., Dickman, R. L., & Huang, Y.-L., 1990, *ApJ*, 352, 139
- Stutzki, J., & Winnewisser, G., 1985, *A&A*, 144, 13
- Toth, L. V., & Walmsley, C. M., 1996, *A&A*, 311, 981
- van der Tak, F. F. S., van Dishoeck, E. F., Evans II, N. J., & Blake, G. A., 2002, *ApJ*, 537, 283
- Womack, M., Ziurys, L. M., & Wyckoff, S., 1992, *ApJ*, 387, 417
- Yang, J., Umemoto, T., Iwata, T., & Fukui, Y., 1991, 373, 137
- Zinchenko, I., Forsström, V., Lapinov, A., & Mattila, K., 1994, *A&A*, 288, 601
- Zinchenko, I., 1995, *A&A*, 303, 554
- Zinchenko, I., Mattila, K., & Toriseva, M., 1995, *A&AS*, 111, 95
- Zinchenko, I., Henning, Th., & Schreyer, K., 1997, *A&AS*, 124, 385
- Zinchenko, I., Pirogov, L., & Toriseva, M., 1998, *A&AS*, 133, 337
- Zinchenko, I. I., 2000, *PAZh*, 26, 933 (*Astron. Let.*, 26, 802)

Table 5. Physical parameters of N₂H⁺ clumps

Source	$\Delta\alpha$ (")	$\Delta\delta$ (")	Axial ratio	$\Delta\Theta$ (")	d (pc)	$\langle\Delta V\rangle$ (km s ⁻¹)	M_{vir} (M_{\odot})	n_{vir} (cm ⁻³) (10 ⁴)	$X(\text{N}_2\text{H}^+)$ (10 ⁻¹⁰)
RNO 1B	6(2)	-1(2)	1.6(0.1)	87(4)	0.36(0.02)	2.0(0.1)	153	11.0	3.5
NGC 281	7(1)	-7(1)	1.6(0.2)	42(3)	0.72(0.05)	2.9(0.1)	611	5.6	4.7
S 187 (1)	6(7)	2(7)	1.7(0.7)	63(13)	0.31(0.07)	1.0(0.1)	29	3.5	3.5
S 187 (2)	199(11)	-79(10)	6.3(29.9)	29(69)					
S 187 (3)	115(8)	-98(9)	1.4(0.6)	81(17)	0.39(0.08)	1.6(0.3)	107	5.9	1.2
G 133.69+1.22 (1)	31(4)	-54(5)	1.9(0.5)	75(9)	0.76(0.09)	3.2(1.3)	793	6.0	1.2
G 133.69+1.22 (2)	171(5)	-168(6)	2.3(1.0)	52(11)	0.53(0.12)	2.0(0.4)	213	4.7	2.8
S 199	12(4)	-14(4)	1.1(0.2)	82(9)	0.83(0.09)	1.4(0.1)	167	1.0	6.0
S 201	31(2)	19(3)	1.7(0.5)	45(7)	0.45(0.07)	1.6(0.2)	123	4.4	1.4
G 173.48+2.45	-3(1)	-9(1)	1.7(0.2)	54(3)	0.60(0.03)	2.6(0.1)	411	6.3	6.7
G 173.58+2.44	-6(3)	-12(2)	1.6(0.2)	72(5)	0.80(0.06)	1.4(0.1)	171	1.1	7.2
AFGL 6366 (1)	2(1)	6(1)	1.8(0.3)	38(3)	0.37(0.03)	2.1(0.1)	170	11.1	2.6
AFGL 6366 (2)	89(2)	57(2)	1.5(0.3)	48(5)	0.47(0.05)	1.5(0.1)	105	3.5	3.9
S 255 (1)	6(1)	46(2)	2.7(0.3)	49(3)	0.60(0.04)	2.6(0.1)	433	6.8	4.5
S 255 (2)	23(2)	-45(3)	3.0(0.5)	56(5)	0.68(0.06)	1.7(0.1)	212	2.3	6.3
S 76E	-27(1)	-18(1)	1.3(0.1)	65(2)	0.67(0.02)	2.7(0.1)	518	5.8	11.4
DR 21 (1)	6(1)	-34(1)	1.4(0.2)	49(3)	0.72(0.04)	3.3(0.1)	826	7.5	12.8
DR 21 (2)	-4(2)	56(3)	1.7(0.2)	75(4)	1.09(0.06)	3.3(0.1)	1200	3.1	10.2
S 140 (1)	61(2)	42(2)	1.2(0.1)	89(3)	0.39(0.01)	1.9(0.1)	140	7.9	7.0
S 140 (2)	7(2)	-8(2)	1.3(0.2)	65(4)	0.28(0.02)	1.9(0.1)	108	15.7	3.5
S 153 (1)	16(3)	19(4)	1.3(0.2)	78(7)	1.51(0.13)	2.5(0.2)	990	1.0	8.8
S 153 (2)	-14(7)	122(6)	1.5(0.3)	110(11)	2.13(0.22)	2.5(0.2)	1400	0.5	5.9
G 264.28+1.48 (1)	16(2)	-26(2)	3.4(3.7)	29(16)					
G 264.28+1.48 (2)	80(5)	-39(7)	2.8(4.4)	36(28)					
G 264.28+1.48	33(3)	-27(1)	8.6(11.7)	37(25)					
G 265.14+1.45 (1)	7(2)	-78(2)	3.6(1.5)	42(9)					
G 265.14+1.45 (2)	-32(2)	2(2)	2.6(0.9)	42(8)					
G 265.14+1.45	-11(2)	-39(3)	5.1(0.8)	73(6)	0.60(0.05)	2.2(0.1)	307	4.7	3.4
G 268.42-0.85	4(3)	-25(3)	1.2(0.3)	50(7)	0.37(0.05)	1.9(0.1)	138	9.0	2.3
G 269.11-1.12 (1)	4(1)	34(1)	1.3(0.2)	46(3)					
G 269.11-1.12 (2)	41(2)	102(2)	1.5(0.4)	46(6)					
G 269.11-1.12	14(2)	52(2)	2.9(0.4)	75(5)	0.95(0.07)	2.7(0.1)	717	2.8	5.4
G 270.26+0.83	-18(1)	22(1)	2.4(0.8)	22(4)					
G 285.26-0.05 (1)	-64(1)	-65(1)	2.2(0.9)	27(6)					
G 285.26-0.05 (2)	-124(2)	-107(2)	2.0(0.8)	38(8)					
G 285.26-0.05	-85(2)	-79(2)	3.6(0.8)	62(7)	1.42(0.15)	2.9(0.1)	1220	1.4	3.5
G 291.27-0.71 (1)	-110(1)	-170(1)	1.2(0.1)	72(3)	0.94(0.03)	2.8(0.1)	777	3.2	4.1
G 291.27-0.71 (2)	-81(1)	-97(1)	1.5(0.2)	32(2)					
G 291.27-0.71 (3)	-31(1)	-50(3)	1.3(0.2)	44(3)					
G 294.97-1.73	26(3)	-14(2)	2.4(0.6)	58(7)	0.34(0.04)	2.4(0.1)	200	17.1	1.7
G 316.77-0.02 (1)	-6(3)	27(2)	2.4(0.2)	108(5)	1.63(0.08)	3.3(0.1)	1890	1.5	11.0
G 316.77-0.02 (2)	130(5)	-37(3)	6.0(1.2)	88(9)	1.32(0.14)	4.7(0.1)	3030	4.4	3.0
G 316.77-0.02 (3)	234(1)	-54(1)	2.2(0.3)	45(3)					
G 345.01+1.80 (1)	39(2)	-34(2)	1.8(0.2)	67(4)	0.69(0.04)	3.3(0.1)	765	7.9	3.9
G 345.01+1.80 (2)	-39(1)	30(1)	1.3(0.1)	72(2)	0.73(0.02)	3.3(0.1)	818	6.9	6.9
G 345.01+1.80 (3)	-116(2)	-23(3)	2.6(1.9)	34(12)					
G 345.41-0.94 (1)	80(1)	-31(3)	3.4(0.5)	81(6)	1.10(0.09)	3.2(0.1)	1180	3.0	2.5
G 345.41-0.94 (2)	-36(4)	-43(6)	1.4(0.3)	112(12)	1.52(0.16)	2.2(0.1)	803	0.8	4.0
G 351.41+0.64 (1)	2(2)	223(2)	1.4(0.2)	76(5)	0.63(0.04)	3.7(0.1)	884	12.1	6.7
G 351.41+0.64 (2)	26(1)	115(1)	1.1(0.1)	81(2)	0.67(0.02)	3.7(0.1)	946	10.6	10.0
G 351.41+0.64 (3)	-1(2)	2(2)	1.4(0.2)	89(5)	0.73(0.04)	3.8(0.2)	1120	9.6	5.3

Table 8. Physical parameters of massive and low-mass cores

Parameter	Massive cores		Low-mass cores			
	Mean	Number	With stars		Without stars	
			Mean	Number	Mean	Number
ΔV (km s ⁻¹)	2.5(0.8)	31	0.5(0.3)	35	0.3(0.1)	25
$N(\text{N}_2\text{H}^+)$ (10 ¹² cm ⁻²)	29(33)	36	8(5)	35	6(3)	25
d (pc)	0.5(0.2)	36	0.14(0.03)	22	0.1(0.02)	13
Axial ratio	1.4(0.4)	47	1.9(0.7)	35	2(1)	19
n_{vir} (10 ⁴ cm ⁻³)	6(4)	36	20(20)	34	12(7)	19
M_{vir} (M_{\odot})	658(604)	36	9(16)	34	3(2)	19
$X(\text{N}_2\text{H}^+)$ (10 ⁻¹⁰)	5(3)	36	3(2)	34	2(1)	18
p	1.3(0.1)	25	1.2(0.1)	9	0.8(0.04)	8
Γ (km s ⁻¹ pc ⁻¹)	0.5(0.4)	27	2(1)	14	2(1)	12
β	0.01(0.02)	27	0.02(0.02)	13	0.02(0.02)	7